



HAL
open science

Europa Ultraviolet Spectrograph (Europa-UVS)

K. D. Retherford, T. M. Becker, G. R. Gladstone, T. K. Greathouse, M. W. Davis, M. A. Velez, M. A. Freeman, S. M. Brooks, S. Ferrell, R. S. Giles, et al.

► **To cite this version:**

K. D. Retherford, T. M. Becker, G. R. Gladstone, T. K. Greathouse, M. W. Davis, et al.. Europa Ultraviolet Spectrograph (Europa-UVS). *Space Science Reviews*, 2024, 220 (8), pp.89. 10.1007/s11214-024-01121-x . insu-04846469

HAL Id: insu-04846469

<https://insu.hal.science/insu-04846469v1>

Submitted on 18 Dec 2024

HAL is a multi-disciplinary open access archive for the deposit and dissemination of scientific research documents, whether they are published or not. The documents may come from teaching and research institutions in France or abroad, or from public or private research centers.

L'archive ouverte pluridisciplinaire **HAL**, est destinée au dépôt et à la diffusion de documents scientifiques de niveau recherche, publiés ou non, émanant des établissements d'enseignement et de recherche français ou étrangers, des laboratoires publics ou privés.



Distributed under a Creative Commons Attribution 4.0 International License



Europa Ultraviolet Spectrograph (Europa-UVS)

K.D. Retherford^{1,2} · T.M. Becker^{1,2} · G.R. Gladstone^{1,2} · T.K. Greathouse¹ · M.W. Davis¹ · M.A. Velez^{2,1} · M.A. Freeman¹ · S.M. Brooks³ · S. Ferrell¹ · R.S. Giles¹ · A.R. Hendrix⁴ · V. Hue⁵ · E. Johnson¹ · J.A. Kammer¹ · A.D. Marinan³ · B. D Mamo^{2,1} · M.A. McGrath⁶ · P.M. Molyneux¹ · E.G. Nerney⁷ · B. Perez¹ · K.B. Persson¹ · S. Pope¹ · U. Raut^{1,2} · R. Rickerson¹ · L. Roth⁸ · J. Saur⁹ · O.H. W Siegmund¹⁰ · J.R. Spencer¹¹ · A.J. Steffl¹¹ · S.A. Stern¹¹ · B.J. Trantham¹ · M.H. Versteeg¹ · J. Winkenstein⁹ · the Europa-UVS Team

Received: 20 February 2024 / Accepted: 29 October 2024
© The Author(s) 2024

Abstract

NASA's Europa Clipper mission is designed to provide a diversity of measurements to further our understanding of the potential habitability of this intriguing ocean world. The Europa mission's Ultraviolet Spectrograph (Europa-UVS), built at the Southwest Research Institute (SwRI), is primarily a "plume finder" and tenuous atmosphere investigation. The science objectives of Europa-UVS are to: 1) Search for and characterize any current activity, notably plumes; and 2) Characterize the composition and sources of volatiles to identify the signatures of non-ice materials, including organic compounds, in the atmosphere and local space environment. Europa-UVS observes photons in the 55–206 nm wavelength range at moderate spectral and spatial resolution along a 7.5° slit composed of 7.3°×0.1° and 0.2°×0.2° contiguous sections. A variety of observational techniques including nadir push-broom imaging, disk scans, stellar and solar occultations, Jupiter transit observations, and neutral cloud/plasma torus stares are employed to perform a comprehensive study of Europa's atmosphere, plumes, surface, and local space environment. This paper describes the Europa-UVS investigation's science plans, instrument details, concept of operations, and data formats in the context of the Europa Clipper mission's primary habitability assessment goals.

Keywords Europa · Europa Clipper · Ocean worlds · Jupiter · Icy moon · Ultraviolet spectroscopy

1 Introduction

Europa has inspired numerous research studies and has captured broad interest, as perhaps best exemplified by the quote relayed by the HAL-9000 character in Arthur C. Clarke's 2010: *Odyssey 2* "All these worlds are yours, except Europa. Attempt no landing there. Use them together. Use them in peace." We describe here the Europa Clipper mission's

Europa Clipper: A Mission to Explore Ocean World Habitability
Edited by Haje Korth, Bonnie J. Buratti and David Senske

Extended author information available on the last page of the article

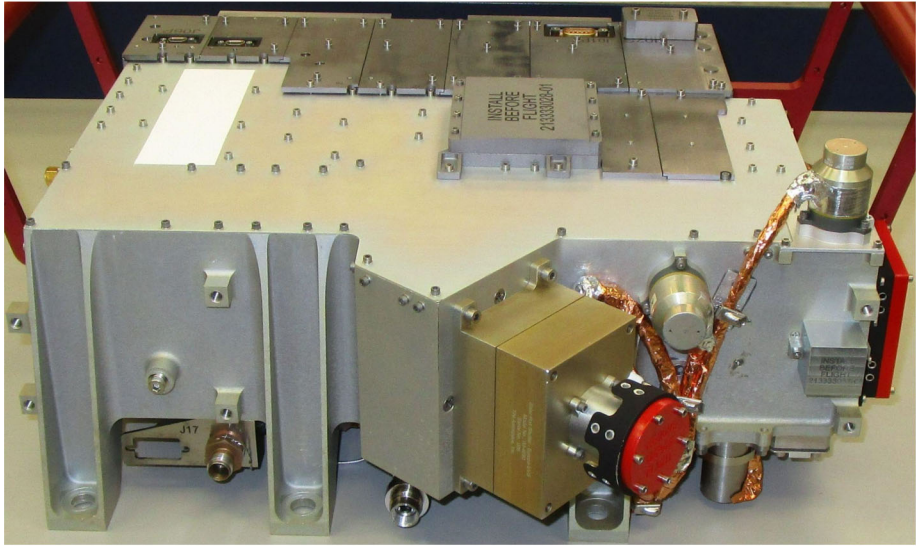


Fig. 1 Europa-UVS photo at time of delivery in February 2022. With dimensions of 36.2 cm × 35.3 cm × 15.8 cm its size resembles that of a briefcase

Ultraviolet Spectrograph (Europa-UVS) instrument and its role in completing the overall goals and objectives for the project, working together with the other instruments on the spacecraft (Pappalardo et al. 2024, this collection). Europa-UVS investigates the interfaces where hard radiation and dense plasmas meet the surface, the atmosphere, and (if present) water vapor plumes to characterize the composition and activity of this potentially habitable ocean world.

As described in Pappalardo et al. (2024, this collection), two of the Level-1 science requirements for the Europa Clipper mission are well addressed by the Europa-UVS investigation, namely: Activity #1 - Search for and characterize any current activity, notably plumes or thermal anomalies, in regions that are globally distributed; and Composition #3 - Characterize the composition and sources of volatiles, particulates, and plasma, sufficient to identify the signatures of non-ice materials, including organic compounds, in at least one of the above forms, in globally distributed regions of the atmosphere and local space environment. Vance et al. (2023, this collection) further detail how these and other mission objectives advance our understanding of the physical and chemical properties that characterize whether Europa is habitable or not.

Europa-UVS is an imaging spectrograph, meaning that both spatial information and spectral information are recorded simultaneously on a detector capturing an image of its long slit's field of view (FOV) after dispersion of extreme-UV (EUV) and far-UV (FUV) wavelengths by its optical grating. Designed, built, assembled, aligned, and calibrated at the Southwest Research Institute (SwRI), the instrument was delivered to the Jet Propulsion Laboratory (JPL) as shown in Fig. 1. The versatility of UV observational techniques, described further in Sect. 3, enables several key science measurements (Sect. 2) as guided by the Europa Clipper project's approach for repeating the simplest set of simultaneous payload observations as possible to reduce complexity.

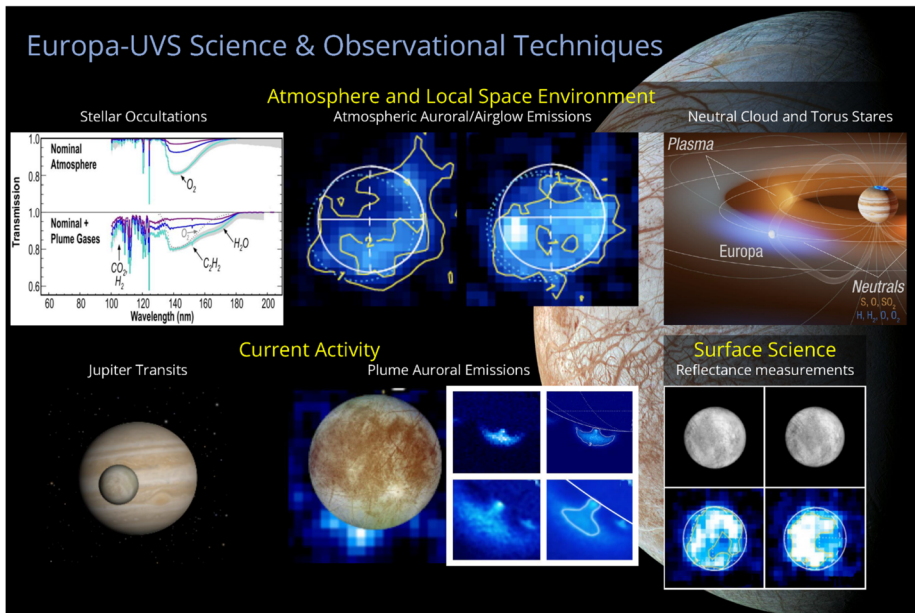


Fig. 2 Europa-UVS science objectives, depicted here, include measuring the composition of Europa’s atmosphere and its interaction with its space environment, searching for and characterizing any sites of active plumes, and far-UV reflectance constraints to surface composition. Image credits: Roth et al. 2014a; Szalay et al. 2022

2 Scientific Objectives

To achieve the baseline Level-1 science requirements for the Europa Clipper mission with Europa-UVS a few dozen measurement requirements were defined and supplemented with additional guidelines to plan the baseline mission. We next summarize the motivation and rationales for these planned measurements and discuss opportunities for additional investigations such as those enabled by joint measurements with the JUPITER ICy moons Explorer (JUICE) mission and its “sister” instrument JUICE-UVS (Retherford et al. 2025). The Europa-UVS science and observation techniques are best summarized in terms of studies of Europa’s atmosphere and local space environment, searching for and characterizing its current activity in the form of plumes, and possibly also through characterizing its surface composition using FUV reflectance spectroscopy (Fig. 2).

2.1 Search for and Characterize the Vapor Composition of Any Plumes

A main science objective of Europa-UVS is the search for ongoing geophysical activity on and above Europa’s surface. The first evidence for geophysical activity in the form of outgassing water vapor plumes was provided through Hubble Space Telescope (HST) observations of FUV emission (Roth et al. 2014a,b) and absorption (Sparks et al. 2016, 2017; Giono et al. 2020), with additional evidence (Blöcker et al. 2016; Jia et al. 2018; Paganini et al. 2020) summarized in Becker et al. (2024, this collection). Water vapor plumes or other outgassing can be observed both in emission and absorption at FUV wavelengths.

Europa-UVS is particularly capable of detecting water vapor emanating from potential plumes at Europa and the dissociation products of that water vapor as a means for achieving

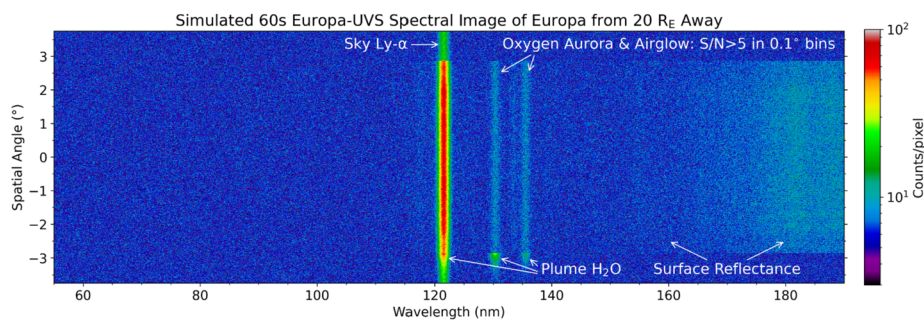


Fig. 3 Proof-of-concept spectral image demonstrating Europa-UVS expected counts per pixel for a nearly filled-slit of Europa's sunlit disk from $20 R_{\text{Europa}}$ away. Reflected sunlight at far-UV wavelengths increases in brightness at longer wavelengths. Simulated atomic oxygen emissions from dissociated O_2 is shown averaged across the disk at expected brightnesses, while both atomic oxygen and hydrogen emissions from dissociated water in a plume source is shown as an example at bottom. Lyman- α skyglow routinely fills the slit as a background source and is also shown at 121.6 nm. Simulated radiation noise counts are included across the entire detector image

the primary goal of searching for and characterizing any plumes (Fig. 3). It is capable of searching for and characterizing the vapor composition of any plumes that extend 30 km or more above the surface of Europa. Measurement requirements specific to the Europa-UVS investigation are designed to ensure it enables Europa Clipper to meet these mission requirements (see Pappalardo et al. 2024, this collection).

Europa-UVS's pushbroom observing method (Sect. 3.7) measures surface, aurora, and airglow features during flybys. These features are also imaged from a distance by scanning Europa's disk, providing observations with the potential to reveal emissions from the water dissociation products within plumes silhouetted against space, as shown by Roth et al. (2014a, 2014b) with data from Hubble's Space Telescope Imaging Spectrograph (STIS). These disk scans will be performed at least six times on the majority ($\sim 70\%$) of Europa encounters, with a sequencing desire of obtaining eight or more such observations on every orbit and including two joint scans with Clipper's other remote sensing instruments. Another measurement requirement (see Pappalardo et al. 2024, this collection) specifies that no fewer than ten Europa transits of Jupiter's disk be recorded by Europa-UVS, with an expectation that more such transit observations are obtained. These observations are a powerful means of detecting telltale absorptions by water vapor and potentially other constituents against the backdrop of the planet all along the limb of Europa. This same observation technique was implemented by Sparks et al. (2016, 2017) and Roth et al. (2017) for investigating Europa's atmosphere and searching for plumes with HST/STIS. In addition, Europa-UVS measurement requirements stipulate that at least 100 stellar occultations be acquired over the course of the mission, and that the coverage of those occultation observations (i.e., those able to determine plume composition and density should an occultation intersect a plume) be distributed globally around Europa. If present at sufficient levels, constituents such as H_2O , CO_2 , O_2 , CH_4 , NH_3 , H_2 , and CO will be detected (Table 2).

Observations of the Sun enabled by Europa-UVS's solar port allows it to obtain additional information on any putative plumes when the mission geometry and sequence scheduling prove favorable for solar occultations. If any plumes occult the Sun from the perspective of Europa Clipper, observations of such an event through Europa-UVS's separate solar port aperture (Sect. 3.2) enables the detection of trace constituents entrained in the plumes with any telltale absorptions at wavelengths shortward of 91.2 nm. Additional

candidate species (beyond those already listed for stars) include but are not limited to H_2CO (see Sect. 3.7.4), and possibly N_2 , C_2H_2 , SO_2 , and O_3 if densities are higher than expected by analogy with Enceladus plumes.

2.2 Enable Mapping of Atmospheric Vertical Structure and Composition

Following the detection of Europa's O_2 atmosphere through the 130.4-nm and 135.6-nm atomic oxygen emission line brightness ratios (Hall et al. 1995), the understanding of its structure (Roth et al. 2016) and additional major constituents such as H_2O (Roth 2021) has been slow in coming (e.g., McGrath et al. 2004, 2009). Aside from the role of water vapor plumes, numerous basic questions remain unanswered about 1) likely hemispherical asymmetries in its global atmospheric density, 2) the scale heights of its main constituents, 3) location of its exobase, and 4) contribution of material to Jupiter's magnetosphere (Bagenal and Dols 2020).

The set of Europa-UVS measurement techniques (Sect. 3.7) described for plume studies, are also adept at characterizing Europa's atmospheric density and temperature structure for each constituent species. Again, these are pushbroom mapping of the surface, airglow, and auroral emissions during the few hours near closest approach, disk scan measurements (both joint with other instruments just before the nadir-pointed pushbroom phase and those repeated when further away), stellar and solar occultations, and Jupiter transit observations. The global perspective that Europa-UVS's remote sensing method provides the Europa Clipper mission works hand in hand with in situ atmospheric measurements, facilitating constraints to 3D atmospheric structure with comparisons to models.

Europa's surface is heavily modified by exogenic processes based on interactions with the charged-particle environment (driven mostly by ions originating from Io) and photolytic processes, and also endogenic geologic processes (including any plume activity). These processes result in compositional variations across the surface that present clues to the geologic and environmental history of the surface, and perhaps also to the subsurface ocean. Through surface sputtering, sublimation, and volatile transport processes, the composition of Europa's atmosphere ultimately traces to its surface composition (Teolis et al. 2017; Becker et al. 2024, this collection). During Europa encounters Europa-UVS scans and nadir-pointed stares are used to understand surface composition and radiolytic and photolytic effects to complement the investigation of atmospheric composition. Water ice is known to be present on Europa's surface (e.g., Carlson et al. 2009); however, the FUV absorption edge at 165 nm (e.g., prevalent at Enceladus and many other icy bodies) remains elusive in HST reflectance spectroscopy observations (Becker et al. 2018, 2022), likely due to contaminants that mask the signature (Raut et al. 2023). We expect that improved spatial resolution with Europa-UVS allows for detection and mapping of H_2O ice concentration across the surface, including potential fresh cryovolcanic deposits not resolved by HST. Salts, sulfur-bearing compounds, organic compounds (e.g., Hendrix et al. 2016) and radiolytic products such as H_2O_2 and O_3 are also detected if present at sufficient abundances. CO_2 ice, where present (Trumbo and Brown 2023; Villanueva et al. 2023), can be distinguished from H_2O ice in the FUV.

Europa-UVS observes Europa's atmosphere at spectral resolutions of 2 nm or less over a wavelength range of at least 60 to 180 nm (Sect. 4.1). This permits the identification of atomic oxygen emission lines at 130.4 and 135.6 nm and atomic hydrogen features at 121.6 nm. To ensure that scans of the atmosphere yield observations with sufficient signal to make compositional and spatial measurements, Europa-UVS has the ability to configure the acquired datasets with variable spectral and spatial bins (see Sect. 3.6) to achieve the required signal quality in each programmable acquisition. Many of the same requirements

levied on plume search observations also ensure that the Europa-UVS atmospheric dataset helps satisfy Europa Clipper mission goals.

2.3 Cross-Cutting Science Objectives

In addition to providing the Europa Clipper mission with a powerful remote-sensing tool for atmospheric, aurora, plume and surface studies, Europa-UVS can be used to address a multitude of other cross-cutting science objectives important to the understanding of the Europa environment and the Jovian System as a whole. Some of these topics include i) constraining the global shape of Europa using stellar occultations (Abrahams et al. 2021), ii) high-energy (>7 MeV) particle flux monitoring (as on Juno, Kammer et al. 2018; Meitzler et al. 2023, this collection; Sect. 3.7.7), iii) neutral torus characterization, etc. It is also likely that the Europa Clipper mission duration overlaps with ESA's JUICE mission (Grasset et al. 2013; Witasse, the JUICE Teams 2020), a mission to study the Jovian system and Ganymede in great detail. The concurrence of both Europa Clipper and JUICE with nearly identical UVS instrument capabilities on these two missions could provide a unique opportunity to understand the Jovian system at a much deeper level than what is obtainable through the individual missions.

Understanding Europa's interior is one of Europa Clipper's fundamental goals, and although Europa-UVS is primarily intended to study Europa's surface and atmosphere, it has the ability to function as a high-precision altimeter (Abrahams et al. 2021). Measuring Europa's global shape precisely with astrometric stellar occultations at 1-ms resolution allows Europa Clipper to test predicted long-wavelength spatial variations in ice shell thickness (Ojakangas and Stevenson 1989) and better understand Europa's interior. In particular, Europa's global shape can reveal this moon's elastic thickness (Araki et al. 2009; Nimmo et al. 2011), interior rheology (Fu et al. 2017), and surface tectonics (Ermakov et al. 2019). Europa-UVS's remote sensing view angles provide constraints to leading and trailing longitudes, and polar latitudes that the Radar for Europa Assessment and Sounding: Ocean to Near-surface (REASON) (Blankenship et al. 2024, this collection) altimetry measurements along the spacecraft ground-tracks will not sample. Combined with Europa Imaging System (EIS) (Turtle et al. 2024, this collection) limb-shape imaging at similar viewing geometries but lower spatial resolution, these measurements improve our general understanding of links to Europa's interior (Mazarico et al. 2023, this collection; Roberts et al. 2023, this collection; Van Hoolst et al. 2024).

To interpret UV emissions from Europa's atmosphere, it is important to understand its plasma environment and plasma interaction. The UV aurora emission, particularly OI 135.6 nm, is generated by electron impact excitation of Europa's O₂ atmosphere. Therefore, observing and modeling the UV emissions from ions in the plasma environment in conjunction with the UV aurora observations will help us understand Europa's atmosphere. Asymmetries in the UV emissions from the atmosphere are strongly controlled by the plasma. For example, the north-south asymmetries and the total UV brightness at different magnetospheric latitudes reported in Roth et al. (2016) are limited by the amount of electron energy being able to get into the atmosphere (Saur et al. 1998). Constraining the plasma interaction is very important as the magnetic field generated by the flow of plasma can be of the same order magnitude or even larger than the induced magnetic fields. Hence, the Europa-UVS measurements, like the Plasma Instrument for Magnetic Sounding (PIMS) (Westlake et al. 2023, this collection) investigation, help further constrain Europa Clipper Magnetometer (ECM; Kivelson et al. 2023, this collection) investigations of ocean induced fields (Kivelson et al. 2004; Schilling et al. 2007). The PIMS investigation provides additional constraints

on the plasma interaction. In situ plasma measurements from one spacecraft would inform the more global view of UV auroral emissions and features seen by UVS from the other spacecraft (see also Retherford et al. 2025).

With the Europa Clipper spacecraft arriving first at the Jupiter system, the JUICE spacecraft can serve en route as a solar wind monitor to investigate connections with Jupiter's magnetospheric phenomenon. There is much speculation about how Jupiter's magnetosphere reacts to solar wind variations (e.g., Fletcher et al. 2023; Hue et al. 2024), but little to no data taken simultaneously from inside and outside Jupiter's magnetosphere exist that could provide decisive conclusions. Most correlations are captured using models of solar wind propagation from Earth out to Jupiter and those are highly uncertain. Understanding the plasma sheet and magnetodisk variability would improve models of the plasma interaction at Europa that creates the auroral emissions targeted by Europa-UVS (Tosi et al. 2024).

The UV reflectance from a surface is controlled by material optical constants, space weathering due to solar UV irradiation and the high-energy electron and ion bombardment, and microphysical properties such as porosity. Thus, measurement of the variations of the surface albedo can inform studies on the chemical composition and age. Observations obtained simultaneously from JUICE-UVS and Europa-UVS with identical solar UV illumination conditions enables more accuracy in the albedo and phase-angle analyses. These attributes, coupled with detailed surface mapping performed by the EIS (Turtle et al. 2024, this collection), Mapping Imaging Spectrometer for Europa (MISE) (Blaney et al. 2024, this collection), and Europa Thermal Emission Imaging System (E-THEMIS) (Christensen et al. 2024, this collection) instruments, can lead to a more complete understanding of the formation and evolution of geologic structures on Europa's surface (Daubar et al. 2024, this collection).

3 Instrument Description

3.1 Europa-UVS Overview

Europa-UVS is preceded by five similar UV spectrograph investigations: 1) Rosetta-Alice explored comet 67P/C-G (Stern et al. 1998; Slater et al. 2001); 2) Pluto-Alice on New Horizons viewed the Jupiter system, Pluto system, Arrokoth, and continues with Interplanetary Medium (IPM) studies (Stern et al. 2005, 2008; Slater et al. 2005); 3) Lunar Reconnaissance Orbiter (LRO) Lyman Alpha Mapping Project (LAMP), launched in 2009, continues obtaining lunar data nearly continuously (Gladstone et al. 2010); 4) Juno-UVS at Jupiter (Gladstone et al. 2017) observed Europa's UV aurora and airglow in 2022–2023 during its extended mission; and 5) JUICE-UVS launched 14 April 2023, with two Europa flybys planned prior to JUICE entering Ganymede orbit (Davis et al. 2020; Retherford et al. 2025).

The UVS instrument (Fig. 4) consists of a single assembly comprising: i) a telescope section, ii) a spectrograph & detector section, and iii) an electronics section.

The UVS telescope feeds a 15-cm Rowland circle spectrograph with a spectral bandpass of 55–206 nm. The telescope has an input aperture $4 \times 4 \text{ cm}^2$ and uses an off-axis parabolic (OAP) primary mirror with 120-mm focal length. The light is then focused onto the spectrograph entrance slit (Fig. 5), which has two contiguous segments with field of view (FOV) shapes of $0.1^\circ \times 7.3^\circ$ and $0.2^\circ \times 0.2^\circ$ projected onto the sky. The purpose of the wider square box at the end of the slit is to accommodate the Sun's 0.11° -diameter viewed near 5.2 AU during solar occultations. The circles at top and bottom are bolt holes for mounting this precision laser-etched metal part.

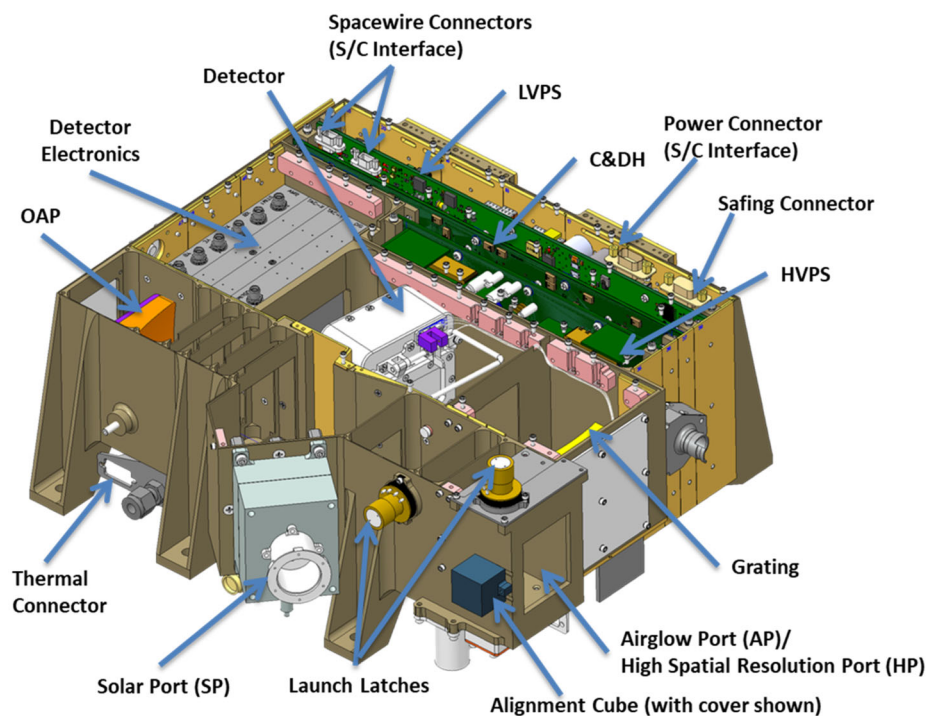


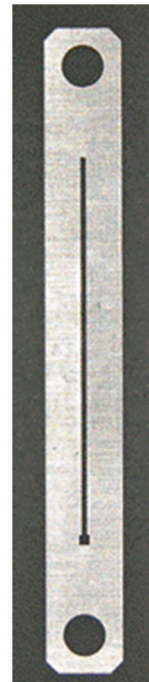
Fig. 4 Europa-UVS optomechanical schematic showing major subsystems, mechanisms, and key components. Figure 7 shows a similar top view of how rays enter the telescope from bottom/right through the AP, HP or SP apertures

Light entering the slit is dispersed by a toroidal diffraction grating that focuses the UV bandpass onto a microchannel plate (MCP) cross-delay line (XDL) detector with a solar-blind, UV-sensitive cesium iodide (CsI) photocathode. Tantalum/Tungsten (TaW) plates contiguously surround the detector and electronics assemblies, shielding the detector and sensitive parts from general particle radiation and high-energy electrons in particular. The detector electronics (DETE) are located behind the detector (Fig. 4).

In a chamber beside the spectrograph are located the Low Voltage Power Supply (LVPS), High Voltage Power Supply (HVPS), and Command and Data Handling (C&DH) electronics boards, connected through a common backplane. The C&DH controls the heater/actuator activation electronics, and event-processing electronics of the DETE.

Europa-UVS builds heavily upon the heritage of the previous SwRI UV spectrographs, especially JUICE-UVS, while incorporating a few modifications for the Europa Clipper mission. First, the detector has been upgraded to feature borosilicate glass microchannel plates (Siegmond et al. 2020), making Europa-UVS less sensitive to secondary gamma radiation created by energetic electrons near Europa. Second, the solar port was further modified from JUICE-UVS so that it is pointed 40° from the main boresight (rather than 60°) for improved accommodation on the Europa Clipper spacecraft. Third, a redundant LVPS was removed to reduce mass by ~ 0.5 kg and operational power by ~ 0.5 W. Finally, the grating has been placed slightly out of nominal spectral focus to improve spatial resolution near 130 nm, at the expense of spatial resolution at wavelengths < 70 nm and overall spectral resolution. This

Fig. 5 Photo of the Europa-UVS slit, showing the combined shape of $0.1^\circ \times 7.3^\circ$ contiguous with a $0.2^\circ \times 0.2^\circ$ box at one end, for a total slit length of 7.5°



change allows greater spatial resolution mapping of Europa's surface and aurora features at long distances than would be possible with the heritage optical configuration.

3.2 Optomechanical Design

The Europa-UVS optomechanical design is the latest evolution of the heritage UVS/Alice design (Davis et al. 2022). The OAP and grating are coated with aluminum and a magnesium fluoride overcoat (Al/MgF_2) to maximize reflection at FUV wavelengths >115 nm while still providing useable throughput at EUV wavelengths 55–115 nm. The toroidal holographic grating has 1600 grooves/mm and a radius-of-curvature of 150 mm in the dispersion plane. The grating blaze wavelength is 90 nm, optimizing diffraction between 55–200 nm. The light dispersed by the grating is focused onto a MCP detector with a XDL anode. The 2D MCP detector is coated with a solar-blind CsI photocathode with responsivity to photon wavelengths up to 206 nm.

Light enters UVS via one of three apertures, depending on the desired observation type: a 40×40 -mm square Airglow Port (AP, the main aperture described previously), a 10×10 -mm square High-spatial-resolution Port (HP), or a 0.25-mm diameter pinhole in the Solar Port (SP). The AP has a door, whose default position is closed while the instrument is powered off. The HP is located in an additional door in front of the AP along the optical path that changes the depth of focus for the instrument to sharpen the spatial resolution while reducing throughput (Davis et al. 2019). Linear Actuator Torque (LAT) motors control both the AP and HP doors and include small magnets to keep them held in position between actuations. The SP is canted $\sim 40^\circ$ from the main telescope boresight to avoid other instrument FOVs when pointing at the Sun, and this angle was minimized to reduce the necessary slew times between apertures (i.e., while still in the general direction of Europa during solar occultations). The SP pickoff mirror is coated with gold, which is $\sim 35\%$ reflective in the UV, then

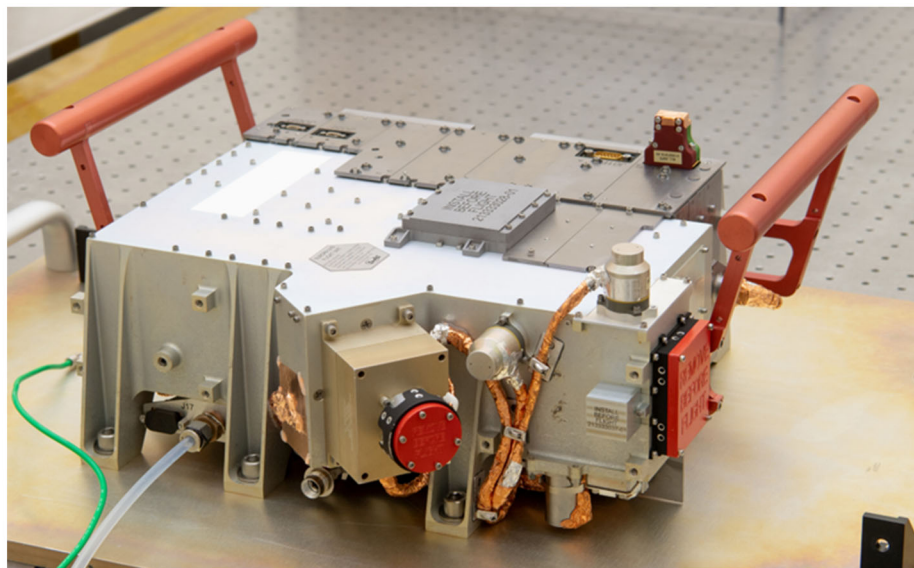


Fig. 6 Photo of Europa-UVS after delivery to JPL. The red handles were removed after attachment to the spacecraft. A mix of internal and external radiation shielding plates are used, with those on the instrument cover shown here at top. Ultra-pure filtered dry N_2 gas enters the instrument through the purge port from the tube at bottom left to maintain instrument cleanliness through the time of launch. The square and circular red tag covers for the AP and SP entrances are removed before launch

overcoated with MgF_2 to reduce reflectance at near-grazing incident angles by a factor of two to three (Raut et al. 2018a) to better match the detector dynamic range. The red-tag handles and covers shown in Fig. 6 (i.e., circular for SP and square for AP) are removed before flight. The Europa-UVS spectrograph section consists of an aberration-corrected toroidal grating that focuses spectrally dispersed light onto the cylindrically curved MCP detector (Fig. 7).

UV optics are especially susceptible to darkening by contaminants such as hydrocarbons deposited on the surfaces and subsequently polymerized. UVS was assembled in an ISO7 clean environment and kept on dry-GN2 purge pre-launch. The mounts for the UVS optical elements (OAP, grating, and SP pickoff mirror) include heater elements to desorb contaminants from their surfaces in flight (Devaud et al. 2018).

Europa-UVS was designed to achieve the measured performance capabilities in Table 1. The final pre-launch ground-calibrated performance (Sect. 4) met or exceeded all requirements needed to realize its science objectives (Davis et al. 2022).

3.3 Detector and Detector Electronics

The Europa-UVS detector configuration (Figs. 4 and 7) consists of three MCPs with $\sim 20\text{-}\mu\text{m}$ pores arranged in a Z-stack. The CsI photocathode is on the top surface of the Z-stack. When a UV photon hits the CsI photocathode, the resulting photoelectron is accelerated down a microchannel, where collisions with the walls produce an avalanche of electrons that emerges from the other end of the Z-stack. The amplified charge cloud leaves the back end of the MCP and is accelerated across the MCP-anode gap, landing on the anode and initiating pulses that propagate in both the +X and -X directions and +Y and -Y

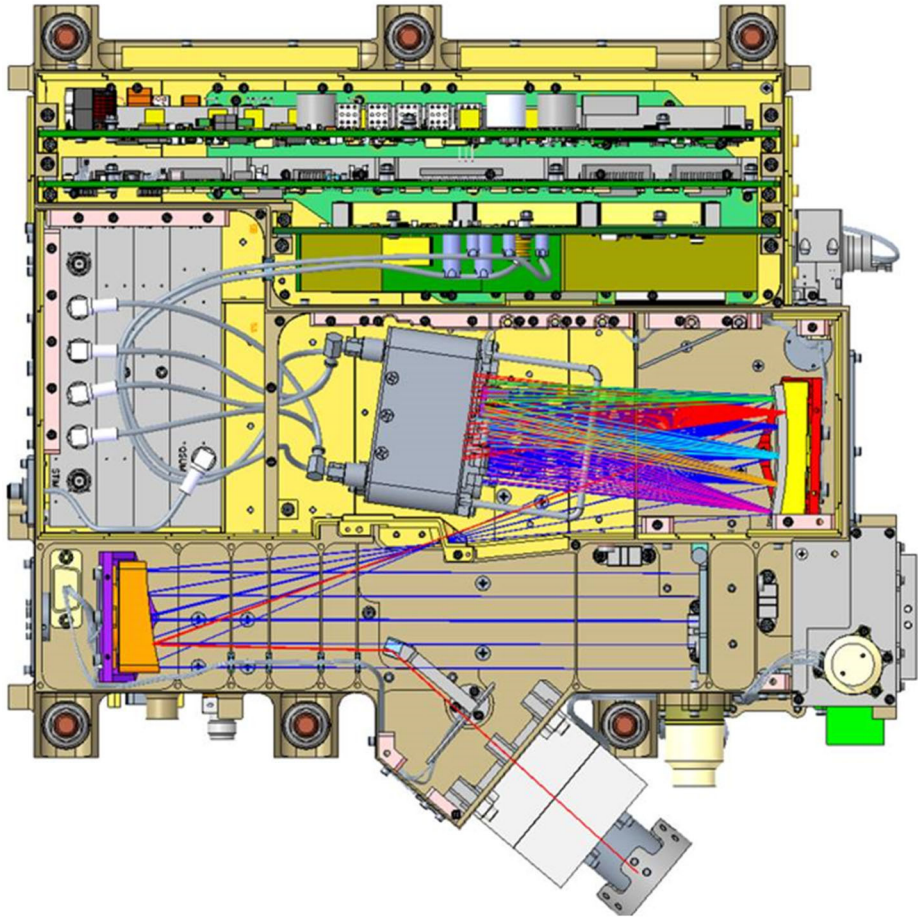


Fig. 7 Europa-UVS Rowland circle spectrograph top-view with ray trace for AP (blue) and SP (red) pathways. See Fig. 4 for labeled subcomponents, mechanisms, and apertures. Light enters the AP from the right, is reflected by the OAP mirror (orange; at left), focused at the slit (where the rays cross near the middle; see Fig. 5 with plate aligned into the page), and reimaged on the grating (yellow) at right. The grating disperses the image of the slit onto the detector (gray; at middle) for each wavelength of light (rainbow of colors here representing the UV spectrum) in first order. Light entering the HP follows a similar path, but with its smaller aperture reducing the throughput of rays and starting a few cm to the right of the rays shown here at the AP door location shown closed here; the HP door is in the open location, mostly obscured in view here. Rays of light entering the 0.25 mm SP pinhole aperture (red) from bottom right, is reflected by a small pick-off mirror (light blue), and follows the same optical path from the OAP, through the slit, to the grating, and then imaged on the detector. The boresight is offset (into the page in this view) to align the SP optical path with the wider $0.2^\circ \times 0.2^\circ$ box part of the physical slit (“bottom” of slit in Fig. 5), but otherwise follows the same path through the telescope and spectrograph sections

directions along integral delay lines to the detector electronics. The detector electronics then output the X and Y centroids of the amplified charge cloud to the C&DH based on the time delay between the two opposing pulses in each axis. The resolution of the x and y position defines the size of the virtual pixel: $19.7 \mu\text{m}$ (X) and $16.3 \mu\text{m}$ (Y).

The MCP material is borosilicate glass coated with atomic-layer-deposited (ALD) magnesium oxide (MgO) (Siegmond et al. 2020). Both the borosilicate glass and especially the

Table 1 Europa-UVS Measured Performance Summary

| Attribute | Measured Performance |
|----------------------|---|
| Bandpass: | 55–206 nm |
| Spectral Resolution: | ~0.6–0.8 nm (center of slit; wavelength dependent) ~1.4 nm (near edge of slit) |
| Spatial Resolution: | 0.15° (near 130 nm at center of slit) 0.29° (near edge of slit and <60 nm) |
| Pixel Plate Scale | 0.0075° ± 0.0002° (spatial); ~0.075 nm (spectral) |
| Peak Effective Area: | 0.26 cm ² (121.6 nm) |
| Mass / Power | 18.84 kg / 7.87 W |

ALD coating result in comparatively minor changes in gain due to charge extraction relative to uncoated lead-glass plates, greatly improving operational lifetime. For example, the LRO-LAMP investigation requires a complicated method to retrieve the total flux at Lyman- α and longer wavelengths where the fluence of photon events on the detector is highest (Grava et al. 2018). Likewise, Juno-UVS steps its high-voltage (HV) levels higher to compensate for the fluence- and time-dependent gain degradation (Hue et al. 2021). JUICE-UVS's MCPs also include the new ALD process to replenish detector gain, but uses lead-glass plates instead.

Each of the three nested MCPs within the Z-stack has a cylindrical 7.5-cm radius of curvature, designed to match the 150-mm Rowland circle diameter for spectral focus and best spatial focus across the Europa-UVS bandpass. The MCP format is 4.6-cm wide in the spectral axis by 3.0-cm height in the spatial axis with a channel length-to-diameter (L/D) ratio of 60:1 per plate. The XDL anode physical size of 4.4 cm × 3.0 cm has an active array area of 3.85 cm × 1.9 cm over which the photons are actively recorded electronically. This active area covers the entire 55–206-nm instrument bandpass in the long dimension (1837 spectral pixels) and 7.5° in the short dimension (~1150 spatial pixels). The approximate resistance per MCP is ~130 M Ω . A 20 lines per inch repeller grid is situated above the MCP photocathode to enhance quantum efficiency by turning escaping photoelectrons back toward the MCP pores.

The XDL MCP is housed in a vacuum enclosure with a door containing a UV-grade, fused-silica window for long-wavelength FUV throughput during testing (and for low fluorescence in-flight). The detector door is spring-loaded for a one-time opening (once in flight) via a wax-pellet actuator. The vacuum enclosure includes a vacuum pump port and a small, polished region that reflects zero-order light from the grating into a light trap on the instrument housing. The vacuum enclosure also has four female connectors for the anode signals and HV connectors for the MCP and anode gap voltages.

The DETE, located next to the detector housing, is composed of five boards: 1) the amplifier board, which comprises two fast amps for the X direction (spectral dimension), two fast amps for the Y direction (spatial dimension), and two charge amps for total event charge; 2 and 3) time amplitude converter (TAC) boards for the X and Y axes, which encode 4096 pixels in the X-axis and 4096 pixels in the Y-axis by event arrival time differences; 4) the digital board (DIG), that provides control signals and interface logic, and 5) a delay-line board to delay the End signals to ensure they arrive with sufficient time-resolution to distinguish the event [x, y] address. The x and y detector addresses of each event are sent to the C&DH electronics for further processing into either a per-pixel list (hereafter, “pixellist”) of event data or an array-totalled histogram (hereafter, “histogram”) of event data at programmable spectral and spatial binning.

The detector electronics also sum analog signals for each event with 8-bit digitization that are used for generating pulse-height distributions (PHDs). The 8-bit MCP pulse-height information, together with the 12 bits of spectral and 12 bits of spatial information, results in a 4-byte output for each event. The pulse-height (charge-cloud amplitude) in a pixellist mode acquisition is available for every single photon event. In histogram mode, however, only the ensemble PHD for the acquisition may be included in the telemetry data. PHDs for pixellist acquisitions can be calculated in ground processing, or a user could filter on the pulse-height value of each event, e.g., to select a subset of events with better quality.

A pulse generator within the detector electronics provides two stimulation (STIM) pixels at two locations in the array. These STIM pixels are useful for both checking data throughput and acquisition modes without the HVPS activated to power the detector, and for correcting the wavelength scale for temperature effects. The mapping of events in physical space to digitally recorded space can vary slightly (e.g., one to two pixels) with detector electronics temperature.

The detector electronics require input DC voltages of ± 6.12 V and +3.3 V. The detector MCP high voltage is raised to a room temperature operational voltage of about -3.55 kV. The gap between the MCP output and the anode array requires a voltage drop of approximately -400 V. Both the MCP and the anode gap voltages are supplied by the HVPS. The average detector gain per photoevent is $\sim 6 \times 10^6$, resulting in a ~ 1 pC charge cloud. At an example average count rate of 2000 count/s, the amount of charge pulled from the MCP as a function of time is ~ 0.008 Coulomb/cm² year. With conventional MCPs, that charge extraction is enough to require an increase of ~ 150 V to maintain equivalent gain; however, with the ALD-coated borosilicate MCPs on Europa-UVS, that charge extraction will not be large enough to trigger a voltage increase to maintain equivalent gain. The gain decreases as charge extraction approaches 0.04 C/cm²/yr, for example, requiring a relatively modest HV increase of ~ 75 V to maintain original gain. While conventional MCPs continue to lose gain as a function of charge extraction, the ALD borosilicate MCPs in Europa-UVS are expected to stabilize after 0.12 C/cm² extracted charge, with no further gain degradation as charge is extracted (McPhate et al. 2019).

3.4 Instrument Electrical Design

The Europa-UVS instrument main electronics are largely single-string but include redundant features for certain important functions. These electronics include a single-string LVPS, redundant actuator electronics, single-string C&DH electronics, a redundant optics decontamination heater system, and single-string HVPS to feed the detector. All of these subsystems are controlled by an 8051-core processor implemented in a radiation-hardened, field-programmable gate array (FPGA) with 64 kbit of fuse-programmable read-only memory (FPROM), 16 Mbit of magnetoresistive random-access memory (MRAM), 128 kbit of static random-access memory (SRAM), and two banks of 16-Mbit acquisition memory. A detailed block diagram of these electronics is shown in Fig. 8.

The change from the dual-string HVPS on JUICE-UVS to the single-string HVPS on Europa-UVS resulted in the opportunity to make use of the space on the unused portion of the printed circuit board for the HVPS. A RadMon hosted RadFET Total Ionizing Dose (TID) dosimeter is used in a total of nine places on the Europa Clipper spacecraft, with one installed on this portion of the Europa-UVS HVPS board (Meitzler et al. 2023, this collection). Being located within the shielded portion of the instrument, only the RadFET chip is included, without the shielded housing for other such hybrid TID radiation monitoring sensors on the spacecraft. A benefit of this dosimeter within the main electronics section is

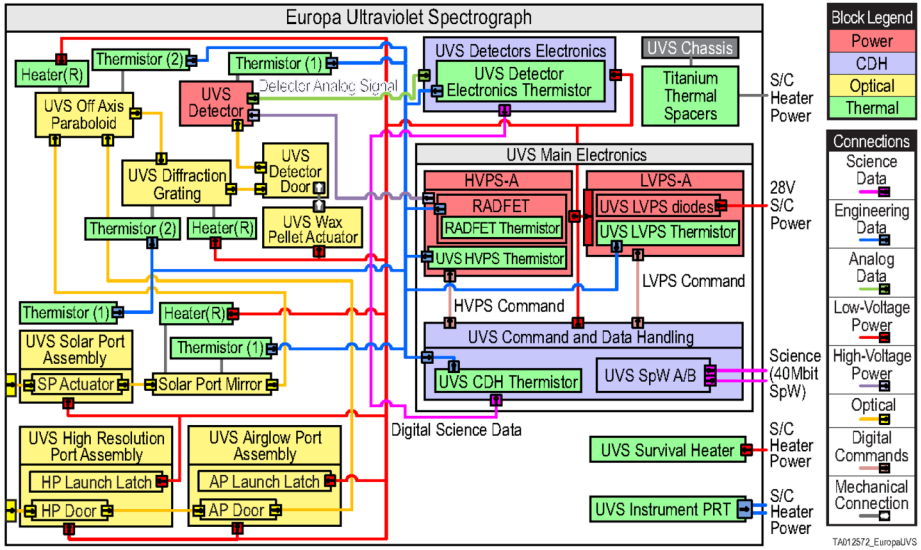


Fig. 8 Europa-UVS functional block diagram. Optical items and assemblies (yellow), thermal heaters and thermistors (green), C&DH and DETE (blue) computer boards, and power boards and the HV-powered MCP detector (red) are color coded subsystems denoted in the block legend at top right. Connections between components are likewise shown using color coded lines and arrows based on the legend at bottom right, including connections with the spacecraft interface on the right side of the block

the ability to verify the radiation model simulations and assessments used to determine the needed tantalum shielding thickness for the instrument (see Retherford et al. 2025 for details on this similar analysis for JUICE-UVS).

3.5 Operations and Data Collection Modes

At any given point in time the Europa-UVS instrument can be in any of five states (including off). Four of these states are operational ones. The different instrument states and associated state transitions are shown in Fig. 9.

Europa-UVS performs a set of periodic safety checks on key parameters when powered on: bright object, HV settings, instrument measured temperatures, etc. When one of these parameters is exceeded (with a configured persistence), the instrument safety is triggered. This trigger changes the instrument state to safe, wherein the internal decontamination heaters are deactivated, HV is deactivated, and the aperture door is closed. These same actions are taken when the instrument is deliberately commanded to the safe state. For example, Europa-UVS is always first commanded to the safe state before the instrument power is switched off to protect the telescope and detector. The spacecraft also performs checks, generating periodic housekeeping packets. For example, the spacecraft measured temperature reference point is checked against the allowable operational temperatures. If any such check fails or there is a general spacecraft emergency, then Europa-UVS is commanded to the safe state and the instrument is nominally powered off after a few seconds (enough to close the aperture door). Europa-UVS autonomously changes from acquire to checkout state when a timed acquisition completes. In this case HV remains on, the aperture door status does not change, and Europa-UVS is immediately ready to start a new acquisition upon command (Fig. 9).

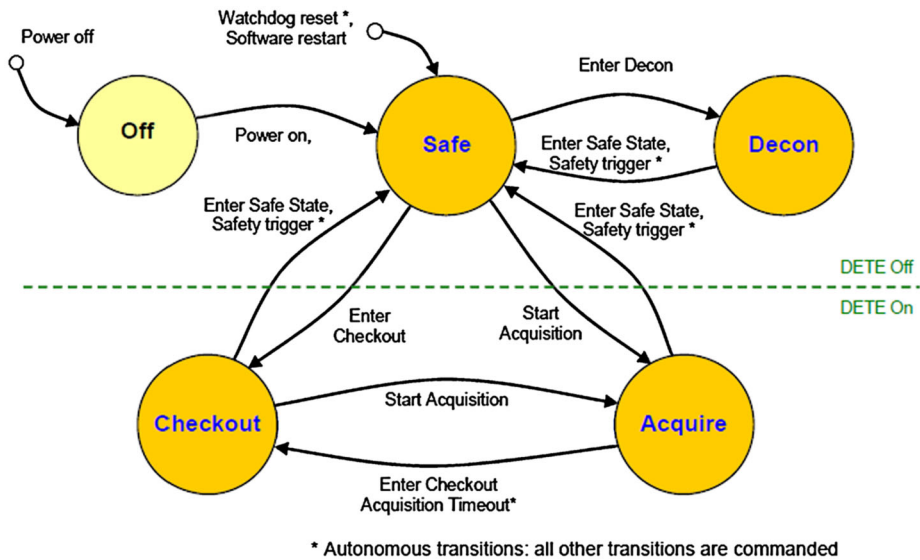


Fig. 9 Europa-UVS instrument state diagram. Three states with the detector off (top) and two states with detector electronics on (bottom) are shown. The “safe” state is both the one entered during a safety-event triggered by an exceedance of a checked parameter (e.g., followed immediately by instrument power-off) and a nominal interim state for Europa-UVS following a power-on commanded by the spacecraft or a state transition commanded by the instrument. Decontamination heaters (“decon” mode) are used periodically for optics cleanliness throughout the mission. Science data is obtained in “Acquire” mode

Europa-UVS implements two main science-acquisition modes: histogram and pixellist. These modes both capture the information from the detected photon events over a specified acquisition period but differ in the way this information is captured and stored for transmission to the ground. The pixellist-acquisition mode captures each detected photon event with a spectral, spatial and pulse-height value and stores these in a list (i.e., [x, y, p-h]), with numerous simultaneous events in a time-resolved interval listed together. The pulse-height amplitude represents a quality of the counting event, and Sect. 4.1.5 for example describes global and local count rate limits and detector dead-time effects known to reduce event qualities. To provide timing information, special entries called time-hacks are added to this event list at a regular specified rate. The histogram mode counts the number of detector events for a well-specified exposure time and duration based on their spectral and spatial coordinates in a 2-D array and can also count the number of detector events based on their pulse-height coordinate in a separate 1-D array. The histogram mode in most cases results in smaller and deterministic data volumes and is expected to be used for the majority of Europa-UVS science observations. The pixellist mode can be considered a raw mode that captures all the information from the detector.

In histogram mode, the maximum time resolution is 10 ms, selectable in 10-ms steps up to 2.55 s and then followed by 1-second steps from 3 s to 18.1 h. In pixellist mode, the maximum time-resolution capability is 1 ms, selectable in 1-ms steps up to 255 ms.

The Europa-UVS detector electronics assign detected photon events in a $4096 \times 4096 \times 256$ array space, where the three dimensions correspond to the spectral, spatial and pulse-height ‘location’ of the detected event. Therefore, each raw detector event is represented in $12 + 12 + 8 = 32$ bits. Within the 4096×4096 addressable spectral and spatial ranges, the active detector occupies an area subset of about 1837×1009 pixel elements, located

around the spectral and spatial positions (“[x, y]”) of top left [1101,2452] and bottom right [2938,1443] measured pre-flight at room temperature. Note however that image distortions near the left and right edges of the detector (i.e., low and high x value columns) result in an active area space on the array that is not a perfect rectangle and with reduced spectral resolution near these edges; compared to heritage UVS/Alice MCP detectors the benefit of accepting these regions of degraded linearity and resolution is ~ 10 nm of expanded band-pass.

As mentioned, the detector electronics also include a STIM (stimulator) fiducial within the detector space that generates artificial events at two locations, allowing for thermal correction of the data. These STIM pixels are outside the detector’s active area and reside near the spectral and spatial positions of [744,3121] and [3198,849], respectively (at room temperature, pre-launch).

After detector events are received from the electronics two simple configurable filtering functions can be applied to reduce the number of invalid events: a discriminator function limiting the accepted pulse-height values, and ten separate defined masks. The discriminators provide an upper and lower limit to the accepted pulse-height value for processing events, allowing us to filter out low pulse-height events marginally detected due to a low detector-gain value, and very high pulse-height events most likely caused by radiation instead of photons. Masking allows us to exclude recorded events in a defined spectral/spatial range (i.e., a rectangle in the detector space) from any further processing, reducing the number of digital events. This may be used to electronically mask out hot spots in the detector or to reduce the data volume, e.g., by excluding any improperly classified events from the edge of the detector. Events are only passed through the masking phase when they fall outside all of the (up to ten) defined rectangular masks, which allows us to apply complex masking patterns if necessary.

In addition to the two main acquisition modes, the instrument can capture several types of count-rate data in parallel or individually. This allows reporting of the total number of counts over a configurable period from 100 ms up to 25 seconds in steps of 100 ms. In addition, any number of the following nine of different count rate product types can be selected for reporting: i) raw (fast, >1 Hz) analog detector, ii) fully captured digital, iii) discriminated, iv) masked, and v) five different spectral-band subsets. Even at the highest rates and most inclusive collection this count-rate data provides only a very modest-sized data volume. Count-rate data can be used for various functions within the system. For example, it could be used as a selector to determine or update the priority for which data should be downlinked. It can track captured analog and digital rates to estimate detector dead-time for calibration (Sect. 4). With the possibility of defining up to five separate spectral bands, this last type of count rate can be used as a low-fidelity science capture mode, capturing just photon rates in a few spectral bands suitable for quick-look assessments (Sect. 6.4). Likewise, one or more spectral bands could be defined to provide a low-rate, high-energy radiation monitor using relevant detector columns expected to be absent of photon-based signals.

3.6 Programmable Acquisition Modes

The histogram and pixellist modes can be configured to tailor the digital selection of spectral and spatial resolution and range of detector area to downlink the desired science information using a minimum of needed data volume per observation. Supported by hardware, each acquisition can be commanded with a set of Lookup Table (LUT) parameters that are custom designed by the Europa-UVS team for each activity type (Sect. 3.7) to return the information subset of interest. We refer to this particular type of windowing and binning

as “programmable acquisition” modes, and this data-volume optimization capability is new relative to the first four UVS/Alice instruments.

After the initial discrimination and masking steps, all the remaining events are converted in resolution and range for each of the spectral, spatial and pulse-height values of the event. The conversions of these three value types are implemented as LUTs that can be filled with any conversion function. The photon events in the detector space are converted to a region of interest in spatial and spectral space (excluding inactive detector space) for the specific science observation being acquired, tailoring the subset of spatial and spectral ranges to remove unnecessary information. Furthermore, the events are also encoded using the minimum number of bits needed for the specific science observation. For pixellist acquisitions, this programming simply reduces the number of bits from the raw 32-bit detector event to a number just sufficient to obtain the measurable quantity of interest (i.e., based on spectral and spatial ranges and resolutions). For instance, if only 1/7th of the inherent raw resolution is needed for 20% of the spectral range on the detector with full resolution on the other 80%, then the events are reduced from 32- to 27-bits.

Note that this lookup-based mechanism enhances operational flexibility by maximizing science return while minimizing data volume. For example, it allows us to select the atomic oxygen emission line wavelength locations at full resolution but sample the longer-wavelength surface reflected sunlight continuum (Fig. 3) at a lower spectral resolution. Histogram exposures can be commanded in units of 10 ms. Such a fast rate for the full array size would result in prohibitively large data volumes. This selectable reduction in spectral and spatial resolutions enables more flexible plans for data acquisitions.

For the histogram acquisitions the system provides an additional data-reduction method in the form of setting a digital image saturation level. As mentioned above, the histogram acquisitions count the number of events for each spectral and spatial coordinate in a 2-D array, where each value is represented as a 16-bit counter, allowing 0 to 65,535 counts to be captured. The counter will saturate at the maximum count in the case when more events are captured during a single exposure in a specific mapped spectral and spatial coordinate. Based on the observation planning, including expected brightness and resolutions, a required dynamic range may be defined that is smaller than the provided 16 bits; for example, a reduced bin depth may be defined at 10 bits, reducing the downlinked data volume by an additional 37%. For instance, in cases where the bright Lyman- α sky feature is of no importance to the specific science goal (e.g., perhaps for relatively dim stellar occultations), the bins capturing those events can simply be left to saturate.

Note that the 2-D histogram array can contain up to one million pixels in memory, which requires undersampling the full $4k \times 4k$ array detector and 1837×1009 active area resolution with these programmable acquisitions. Pixellist data mode is required to capture the full array at full resolution.

3.7 Science Operations Activity Types

The Europa-UVS investigation will achieve its scientific requirements through a series of activity types. Each activity is designed to address specific science goals; however, the activities are not limited to a single detector setup where all detector regions are recorded equally. Instead, they can be programmed to achieve any combination of spatial and spectral resolutions (i.e., full or reduced), exposure times, etc. as described in Sect. 3.6. This flexibility within each activity allows for the science objectives to be met while optimizing the required data volume resource.

3.7.1 Europa Surface, Aurora, and Airglow Stares

The majority of the science operations for Europa-UVS will be conducted while the instrument is nadir-pointed. This activity type is referred to as the Europa Surface, Aurora, and Airglow (SAA) stares. The SAA stares nominally occur for the duration of the flyby while the spacecraft is at an altitude $<165,000$ km from Europa, except when other Europa Clipper activities occur (including other Europa-UVS activities). The airglow and aurora measurements provide information on both bulk molecular (O_2 and H_2O) and trace atomic species in the atmosphere. The long duration series of these observations is needed to constrain how the gas distribution and variable auroral emissions are coupled to the inhomogeneous plasma environment, providing the required baseline to interpret more sporadic events such as potential plume emissions. During closest approach ($<40,000$ -km altitude), the SAA stares acquire high-spatial-resolution spectral images of the surface that can be used to correlate UV surface features with their composition and any fine-scale UV aurora features to search for inhomogeneities in the local atmosphere (e.g., plumes and vents) or plasma flow (e.g., such as electron beams). The atomic oxygen emissions are continuously present and sufficiently bright to be measurable during all observations. Longer stare observations or coadded data will search for fainter trace species such as S, C, or CO. The spectral and spatial resolutions of each stare can be programmed as needed during each encounter. This includes changing the spatial resolution along the slit length as the apparent size of Europa changes, focusing on select spectral features, and accounting for nightside (low-light) observations. A repeated series of images at each resolution setting results in an image-cube type data product.

3.7.2 Europa-UVS Scans

The Europa Clipper spacecraft is slewed to conduct multiple “scans” by pointing the Europa-UVS slit across Europa at a constant angular rate in the across-slit direction over approximately 10 minutes. The 10-minute scan begins and ends approximately $\pm 1.5 R_{\text{Europa}}$ away from Europa’s center to capture any extended auroral and airglow emissions above the limb. The scans enable the long, yet narrow, Europa-UVS slit to build up a complete composite image over an entire hemisphere of Europa, resulting in a relatively high-resolution snapshot of the aurora across Europa and a spectral/spatial map of the surface. The scan is complementary to the much longer SAA stares that only partially capture Europa and its aurora when the angular size of Europa exceeds the 0.1° -wide slit.

During most Europa encounters, four scans are nominally scheduled to occur during approach and four scans are scheduled during departure, with <2 hours between each scan. Each set of four (or at least three) scans nominally occurs within a period less than or equal to $1/2$ the Europa-Jupiter synodic period (~ 5.6 hours), e.g., covering the time from one plasma sheet crossing to the next. This cadence is designed to observe the intrinsic variability of the auroral morphology over the Europa–Jupiter synodic period, which provides global information regarding the plasma environment and its interaction with Europa as modified by the induced magnetic fields and by the subsurface ocean.

At a distance of $\sim 40,000$ km from Europa on approach and departure, the Europa Clipper spacecraft will perform a “joint scan” during which multiple remote sensing instruments, including Europa-UVS, are operating. The joint scan is similar to the more distant Europa-UVS scans, except for a slightly longer duration on-disk to optimize the signal quality for all instruments during the activity. As available, our data collection method also allows acquisitions while slewing off- and back-to-nadir during the setups for these scans, albeit with a more complicated time-based reconstruction.

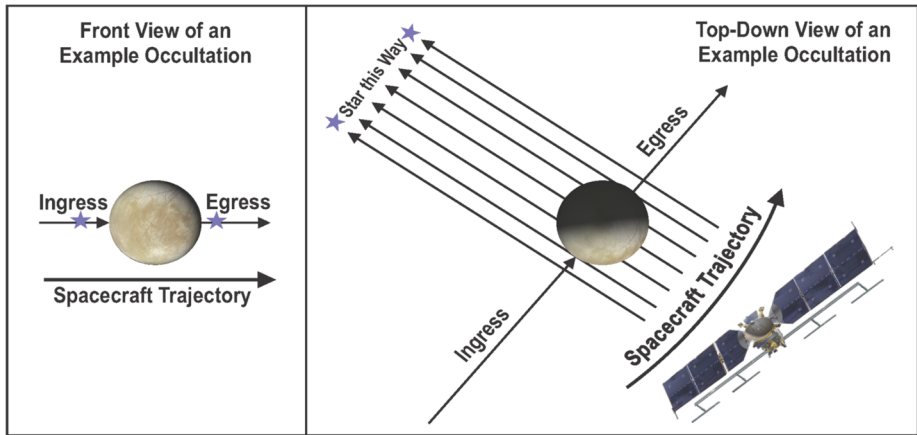


Fig. 10 Occultation geometry sketch, viewed from Europa Clipper as shown at left. With inertial spacecraft pointing towards a star, Europa moves into (ingress) and out of (egress) the UVS field of view based on the spacecraft velocity along its trajectory as shown with a top-view at right. The angular velocity of Europa's tangent point along these lines of sight determines the available exposure time per atmospheric scale length of interest, based on the tangent point altitude rate of change. Gases around Europa attenuate the starlight as a function of wavelength, leaving a potentially discernible fingerprint in the stellar photons observed with Europa-UVS

3.7.3 Stellar Occultations

Europa-UVS performs a minimum of 100 observations of stellar occultations by Europa to characterize its atmosphere and search for plumes. This activity involves centering the slit on a UV-bright star when that star passes within 150 km ($\sim 0.1 R_E$) of Europa's limb from the spacecraft's perspective (Fig. 10). The primary goal of the stellar occultation activities is to identify and map the vertical distribution of atomic and molecular species in Europa's thin atmosphere. The data set will constrain column density, spatial distribution, and temporal variations of these atmospheric constituents (e.g., O_2 , H_2O , CO_2 , H_2 , O , H ; Hansen et al. 2020 report the complete set of Cassini UVIS measurements of H_2O column density in Enceladus' plume, for example). The observations are planned to be distributed in latitude and longitude such that at least one occultation occurs over each of Europa's 14 identified surface panel regions (Pappalardo et al. 2024, this collection). Stellar occultation observations are designed to achieve a 50-km scale height resolution in order to adequately probe the vertical structure of the atmosphere with good data quality, with this resolution improving to at least 30-km for characterizing the composition of any plumes, if detected.

Stellar occultations can be observed during ingress (the star is observed prior to being occulted by Europa) or egress (the star is observed after emerging from behind Europa). Europa-UVS also observes grazing stellar occultations (appulses), when the star crosses behind Europa's atmosphere but is never blocked by Europa itself. In all three cases, the occultation observations are designed to acquire a baseline of the unocculted stellar signal for direct comparison with the occulted stellar spectrum as a function of distance to Europa's surface. Stellar occultations can also probe the exact shape and size of Europa, constraining the topography with a precision on the order of meters when measuring the surface intercept point at 1-ms time resolution (Abrahams et al. 2021). Observing both ingress and egress for a given occultation event provides higher accuracy.

The Catalog of UV Bright Stars (CUBS) was created (Velez et al. 2024) to select the set of stars for the planned occultations. Consisting of $\sim 90,000$ stars, CUBS provides spectra for each star by using IUE (International Ultraviolet Explorer) observational data where available (1746 stars) and Kurucz models elsewhere (Castelli and Kurucz 2003, 2006). Every potential occultation is run through a prioritization scheme to rank its quality. The scheme starts with a numerical analysis of the estimated signal-to-noise ratio (SNR) for each star contingent on its brightness in the UV bandpass of O_2 absorption (130–175 nm) and the speed of the star relative to Europa from the spacecraft's point of view (Fig. 10). Figure 11 shows simulated stellar and solar spectra at different tangent point altitudes and the SNR per resolution element derived for the normalized transmission spectra in expected average cases. After assigning each occultation a quality factor of "Very Good", "Good", "OK", and "Bad", each candidate event is further analyzed using a list of subjective criteria to increase or decrease its rank accordingly (Velez et al. 2024). For example, "Good" events that might be coordinated with JUICE-UVS observations would be increased to "Very Good" in the priority scheme. For another example, any occultation opportunity viewing a line of sight that passes near the spacecraft trajectory's footprint on the surface would be of value for direct comparisons with in situ measurements by the MASS Spectrometer for Planetary Exploration/Europa (MASPEX) and SURface Dust Mass Analyzer (SUDA) instruments (Waite et al. 2024, this collection; Kempf et al. 2024, this collection). Events with $SNR < 3$ are "Bad" and not considered further. See Sect. 5 for a more complete list of criteria considered during instrument operations planning.

The molecular oxygen (O_2), water (H_2O), hydrocarbons (C_xH_y), and other species of interest are all detectable by Europa-UVS using these occultations during the entirety of the mission. The SNRs in Fig. 11 and Table 2 assume a case with H_2O column density of 2.31×10^{-15} at 80 km altitude for the stellar occultation and 4.17×10^{-14} at 100-km altitude for the solar occultation simulations. The mixing ratios of constituents relative to water are assumed to be those for Enceladus' plume (Waite et al. 2006, 2017). Most, but not all, species considered are detectable in one or more scenarios with various integration time intervals in each case.

3.7.4 Solar Occultations

Solar-occultation observations are similar to stellar occultations, except the occulted light source is the Sun rather than a distant stellar point-source. The benefits of solar occultations are their increased signal-to-noise and ability to observe atmospheric absorptions of light at wavelengths < 91.2 nm, which are not covered by the vast majority of stellar occultations because those wavelengths are typically absorbed by the interstellar medium. Solar occultations better constrain the column densities of several trace species, with several example species listed in Table 2. To enable solar occultations, the Sun is observed through the solar port (Sect. 3.2), whose boresight is designed to place the Sun in the $0.2^\circ \times 0.2^\circ$ box at one end of the instrument's slit-defined FOV (Fig. 5). These occultation observations are designed to typically last ~ 10 minutes during either the ingress or egress portion of the occultation, depending on the availability to schedule a spacecraft pointing maneuver in the planning sequence.

3.7.5 Jupiter Transits

Jupiter transits provide detailed information about the atmospheric composition and structure around the entire limb of Europa. These activities use Jupiter as the background illumination source to constrain the column density, global spatial distribution, and temporal

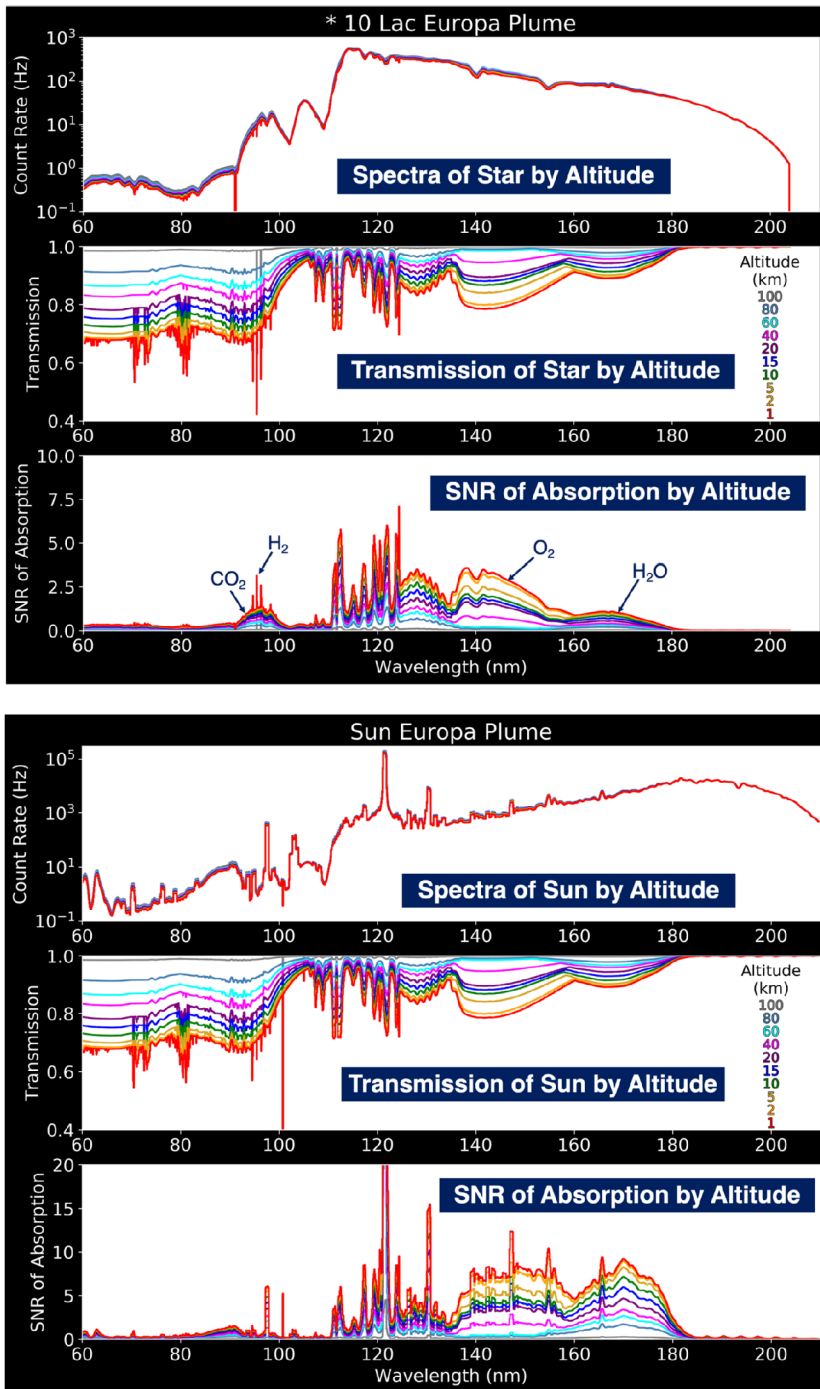


Fig. 11 Proof-of-Concept Stellar (top) and Solar (bottom) occultation spectra, transmission spectra, and SNR per resolution element. The star used in this example has a Europa-UVS signal rate of ~15,000 counts/s. For both examples, we use a 1-second time resolution at each altitude level

Table 2 Expected signal-to-noise ratio (SNR) and sensitivity to various species of interest using stellar and solar occultations over different time resolutions at 1 km above the surface

| Component | SNR @ 1 s (Star/Sun) | SNR @ 10 s (Star/Sun) | SNR @ 100 s (Star/Sun) |
|-----------|-------------------------|--------------------------|---------------------------|
| H_2O | 52/330 | 160/1040 | 490/3100 |
| O_2 | 45/120 | 140/390 | 430/1200 |
| H_2 | 4.1/5.3 | 133/17 | 39/52 |
| C_2H_2 | 0.008/0.025 | 0.024/0.079 | 0.071/0.23 |
| NH_3 | 0.91/3.8 | 2.8/12 | 8.4/35 |
| CH_4 | 1.3/5.1 | 4.0/16 | 12/47 |
| CO_2 | 5.9/6.0 | 19/19 | 55/56 |
| H_2CO | 0.41/1.5 | 1.3/4.8 | 3.8/14 |
| CH_3OH | 0.019/0.071 | 0.06/0.22 | 0.18/0.66 |

variations of the primary atmospheric constituents of Europa (i.e., O_2 and H_2O) and for hunting multiple plume locations around the limb, similar to the technique used to make putative plume detections by Sparks et al. (2016, 2017). The activity occurs in two primary ways: (1) the Europa-UVS FOV is pointed at Jupiter while Europa passes through the slit center; and (2) one or more scanning activities are conducted while Europa is passing in front of Jupiter. This activity occurs on the daylit side of Jupiter (e.g. solar phase angle less than 120°) a minimum of 10 times throughout the mission. When possible, the observations target Europa at times when viewing the brighter subsolar or Lyman- α bulge regions of Jovian dayglow emissions.

3.7.6 Neutral Cloud and Torus Stares

Io's volcanic source of predominantly neutral SO_2 is the ultimate origin of the Io plasma torus and majority of Jupiter's magnetospheric plasma. Material from Io's atmosphere is both ionized, picked-up, and then swept away by Jupiter's magnetic field, and also ejected as neutrals to form an extended neutral cloud that is shaped via gravity and electromagnetic interactions (Bagenal and Dols 2020). This extended source of neutral atomic sulfur and oxygen is ionized into sulfur and oxygen ions (S^+ , S^{++} , S^{+++} , O^+ , and O^{++}), again producing magnetospheric plasma that is subsequently transported to Europa. This corotating plasma is excited to higher-energy states via electron impact excitation; then, through spontaneous emission of forbidden transitions, it decays back to a lower-energy state, emitting UV light that indicates plasma conditions (Steffl et al. 2004; Nerney et al. 2017). By measuring these UV emissions routinely at Europa's position and occasionally more system-wide, Europa-UVS is able to investigate Io as an exogenic source of sulfur implanted on Europa's surface and also to characterize the variability of Europa's plasma environment.

The strongest Io plasma torus emission lines in the UV are at 68.0 nm due to S^{++} and at 83.3 nm / 83.4 nm due to a combination of O^+/O^{++} emission lines. The neutral sulfur and oxygen atoms that form the extended neutral cloud are also excited via electron impacts that cause emission in the UV. Under typical plasma and solar conditions, solar-resonant scattering is also thought to be responsible for $\sim 1/3$ rd of the 130.4-nm neutral oxygen emission.

Europa-UVS's neutral cloud and torus stares are designed to constrain the strength of Jupiter's plasma environment and interaction with Europa's conductive ionosphere and related current system. This information supports the PIMS instrument (Westlake et al. 2023,

this collection) and Europa Clipper Magnetometer (ECM; Kivelson et al. 2023, this collection) measurements by characterizing the influence of plasma-induced fields as distinguished from ocean-induced field perturbations.

The neutral cloud and torus stares are nominally scheduled at the beginning of approach phase and end of departure phase for each of the Europa encounter orbits, occurring ~ 1 – 1.5 days from closest approach. Nominal integration times are set at 30 minutes for these diffuse emission observations. Europa is targeted but the range is so large that Europa is not spatially resolved and Europa-UVS's 7.5° slit covers up to a few Jupiter radii in extent, with a typical torus or cloud scale height being ~ 0.5 Jupiter radii. Based on Europa neutral cloud models (Smith et al. 2019, 2022), the CHIANTI database (Dere et al. 1997) for electron impact rates expected in the torus (Nerney et al. 2017; Nerney and Bagenal 2020), and g-factors for solar resonant scattering the total expected ~ 0.2 and ~ 0.04 Rayleigh line brightness for the 130.4 nm and 135.6 nm oxygen features, respectively, are detectable with slit-integrated spectrum peaks of ~ 220 counts/pixel and ~ 40 counts/pixel, respectively, despite the relative faintness of this feature.

When not impacting other activities (e.g., in the year prior to Europa Campaign 1; Pappalardo et al. 2024, this collection), the slit is aligned parallel or perpendicular to the local centrifugal equator of the plasma torus to gather the most information, with optimized deconvolution of line-of-sight density projection effects (i.e., ‘peeling the onion’ by fitting outer radial layers then moving inwards) or determination of effective ion-scale heights and ion parallel temperatures (parallel to magnetic field line) respectively. Matching models of the torus and neutral cloud emissions to the observations allows us to determine ion, electron, and neutral atom densities, and electron temperatures, and how they vary over the line of sight.

3.7.7 Radiation Observations

Nearly all of Europa's science activities naturally also collect information about Jupiter's radiation environment through the observed impact on the detector and the noise measurements within the data (Fig. 12). There are also designated radiation observation activities that occur pre- and post-flyby, nominally outside of the primary subphase time range when UVS scanning observations occur. During radiation observations, the Europa-UVS aperture door is closed, similar to a “dark” calibration (Sect. 4.1.4 and Sect. 4.2), in order to measure the high-energy electron and gamma-ray counts that penetrate through Europa-UVS while within $20 R_J$ of the planet. Each radiation observation lasts approximately one hour. These observations measure the radiation environment near Europa in addition to providing a characterization of the instrument's background noise, complementing Europa Clipper's other radiation environment studies (Meitzler et al. 2023, this collection).

4 Calibration

4.1 Ground Calibration

Following assembly, alignments, and environmental testing, and prior to delivery to JPL for integration onto the Europa Clipper Spacecraft, Europa-UVS was subject to a series of tests to characterize its radiometric performance. These tests included (1) dark-count measurements, (2) spatial point-spread-function (PSF) and wavelength calibration, (3) stray-light rejection, and (4) instrument sensitivity expressed as effective area. These measurements

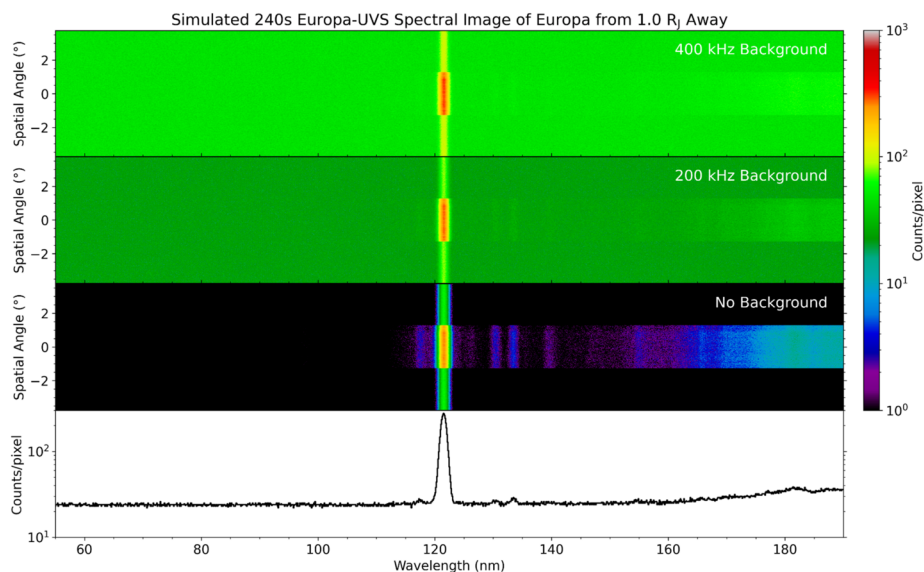


Fig. 12 Proof-of-Concept spectral image with radiation noise shown for different cases. The bottom panel shows total counts integrated across the disk of Europa for an example case with 200,000 counts per second of dark background noise signals from the radiation environment; key features remain detectable

were performed in the Ultraviolet Radiometric Calibration Facility (UV-RCF) at SwRI, as initially reported in Davis et al. (2022).

The UV-RCF system (Davis et al. 2014) is comprised of a differentially pumped Hollow Cathode Lamp (HCL) that uses arc discharge to excite various gases (typically He, H₂, Ne, Ar, CO₂, and mixtures thereof) to generate a broad spectral output overlain with a plethora of narrow emission lines over the Europa-UVS 55–206-nm bandpass. These emission lines are critical for Europa-UVS wavelength calibration. Light from the HCL is fed to a dispersive monochromator (Acton VM-502), which can be operated in different grating modes to relay the light (broadband or at desired wavelengths) to a four-inch OAP mirror. The OAP steers a collimated beam down the beamline towards the high-vacuum chamber that hosts Europa-UVS on a four-axis tip/tilt motorized stage. This stage allows for accurate on- and off-axis alignments of the Europa-UVS apertures (airglow port + solar port) with respect to the incident beam essential for determining spatial resolution/PSF characterization.

Owing to a slight shifting of the optical alignment cube during the curing of its epoxy mounting to the side of the instrument housing, the resulting alignment of Europa-UVS is (very accurately) shifted by $\sim 0.5^\circ$ in the along-track direction relative to the spacecraft nadir alignment coordinate system. As such the Europa-UVS slit falls outside of the default centered EIS-NAC FOV and likely also between two of the E-THEMIS FOVs. This alignment offset will be remeasured once in flight. While within required specifications, this instrument offset is expected to have several implications for the flyby sequencing before and after the nadir-phase occurring $\sim \pm 2$ hours from closest approach.

The photon beam can be intercepted by a NIST-calibrated photodiode (Optodiode AUX-100G) mounted on a retractable linear stage to measure the absolute flux and intensity profile of the beam within the beamline. Knowledge of the absolute flux is essential to measure the effective area. The optomechanical layout of the UV-RCF can be found in Davis et al. (2014). The entire beamline is evacuated with oil-free turbomolecular and non-evaporating

getter (NEG) pumps to $\sim 10^{-7}$ Torr. The main chamber hosting Europa-UVS is cryopumped to $< 10^{-8}$ Torr during calibration runs.

4.1.1 Wavelength Scale

The Europa-UVS wavelength calibration is derived from measurements of the emissions from multiple calibration gases. Images of emission-line features from these gases (Fig. 13) served to determine the spatial and spectral resolutions and the wavelength calibration. Twenty-four different lines produced by the three calibration gases form the basis of the wavelength solution. Variations in position across the slit (spectral direction) were corrected by comparing the relative position of Lyman- α and specific aluminum emission-line features present in all images (Fig. 13; solution at $y=1950$). The cubic fit determines that the pixel scale varies from 0.065 nm to 0.085 nm across the detector, meeting the requirement of $\leq 0.09 \pm 0.01$ nm/pixel. The cubic fit linear approximation is $0.080000x - 27.19$ at $y=1950$, varying slightly over spatial position (Fig. 14).

The total wavelength bandpass across the detector active area is computed with the measured plate scale and offset values. The active area covers spectral pixels 1101 through 2938, corresponding to a total wavelength bandpass of 55–206 nm. This bandpass exceeds the instrument specification for a minimal bandpass of 60–180 nm with margin.

4.1.2 Effective Area

The effective area quantifies the effective collecting area of the instrument given the combined efficiencies of the optical and electronic elements. It translates the conversion efficiency of an incident flux of photons at the front end of the instrument into a detectable electronic signal at the back end of the detector. The effective area of the Airglow Port (AP) and Solar Port (SP) are given by:

$$E_{\text{AP area}} = AS \times R_{\text{OAP}} \times R_{\text{Grating}} \times G_{\text{eff}} \times QE \quad (1)$$

$$E_{\text{SP area}} = AS \times R_{\text{SP}} \times R_{\text{OAP}} \times R_{\text{Grating}} \times G_{\text{eff}} \times QE \quad (2)$$

where AS is the aperture size (16 cm²); R_{OAP} is the reflectance of the MgF₂-coated Al OAP mirror; R_{Grating} is the grating reflectance; G_{eff} is the grating efficiency; and QE is the detector quantum efficiency. The solar port has an additional bounce on a MgF₂-coated Al mirror with an Au coating and is characterized by a reflectance R_{SP} . The lab-measured effective areas for the airglow (Fig. 15) and solar (Fig. 16) ports are shown relative to defined requirements as a function of wavelength. Figure 17 displays these quantities, as well as the resulting effective areas for the airglow and solar ports based on these equations (1&2). The OAP mirror reflectance measurements were provided by Teledyne Acton Optics from 115–400 nm and are shown in dashed blue on Fig. 17a. At wavelengths shorter than 115 nm, R_{OAP} is taken as the theoretical reflectance for a 25-nm-thick, MgF₂-coated Al mirror from IMD modeling (Windt 1998). The same coating is used on the grating, so R_{Grating} is matched to R_{OAP} . The grating equation is used for G_{eff} in Fig. 17b and set to the designed blaze angle of the optic. The as-delivered detector QE spectrum is shown in Fig. 17c. We compare the theoretical effective area with the measured one in Fig. 17d and e. A linear interpolation was used within the measured wavelength range (121.7–167 nm). Outside of this range, we extrapolated based on the theoretical effective area.

Although the use of ALD-coated borosilicate glass in the MCPs has resulted in a detector with excellent dark rate background signals, less sensitive to secondary gamma radiation

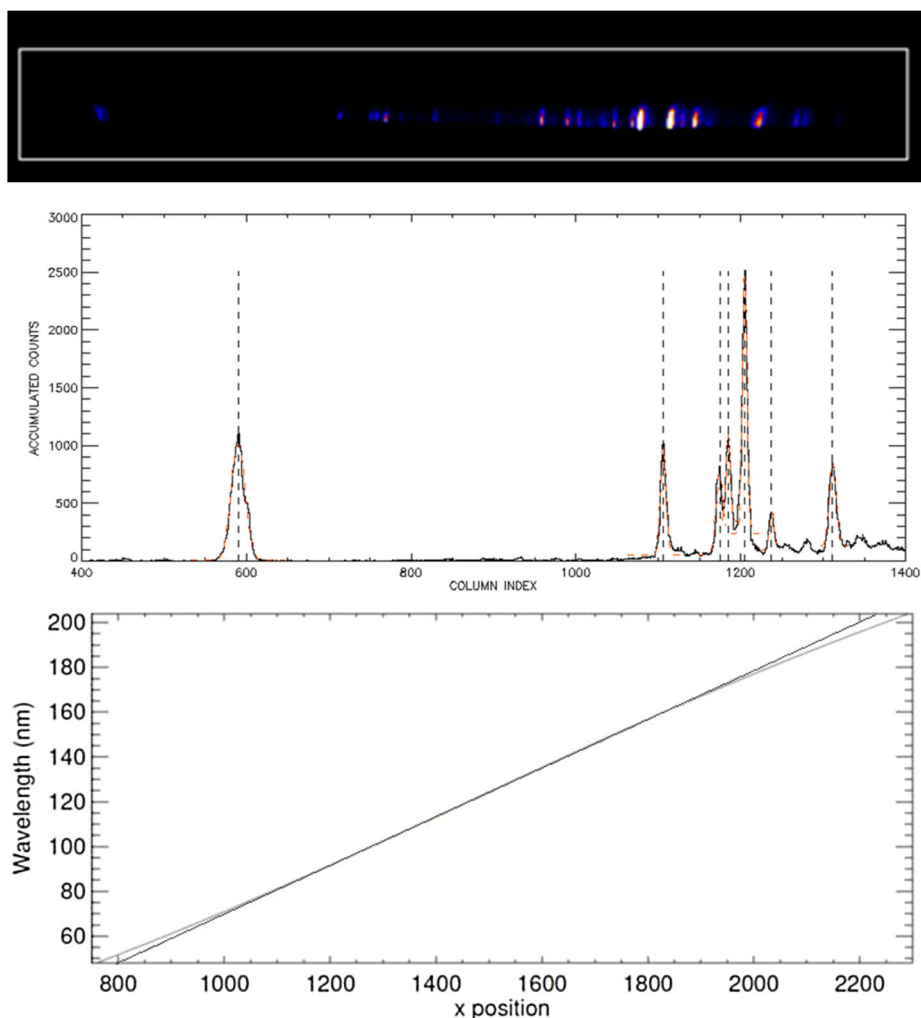


Fig. 13 Europa-UVS ground-based wavelength calibration. An example image (top) and spectral plot (middle) of a Ne spectrum using an input collimated point source to Europa-UVS at slit center. A mapping of the wavelength to detector x position is shown for an example $y=1950$ position near the boresight, with the thinner (and darker) straight line illustrating the deviations from a linear spectral plate scale near the left and right detector edges (bottom)

created by energetic electrons than leaded-glass MCPs, the resulting detector QE (Fig. 17c) performance was less than predicted. While Fig. 15 shows that the Europa-UVS effective area meets its minimum requirements, a comparison with Fig. 17e shows up to ~ 3 times lower responsivity than initially expected in the 120–200 nm range. As a result, our plans for disk scans have implemented slower slew rates to ensure longer exposure times per resolution element, for example, in addition to longer exposure times and other observation plan adjustments to ensure data product quality adequacy (as included in pre-launch science requirement validation tasks).

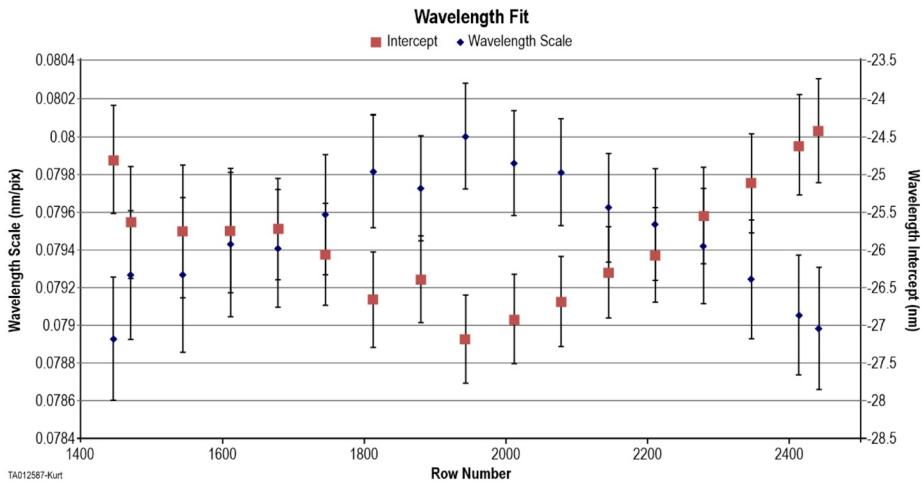


Fig. 14 Wavelength linear scale in nm/pixel (blue triangles) and wavelength intercept from a cubic fit in nm (red squares) as a function of spatial row

As shown in Fig. 16 the SP effective area is lower than specifications for wavelengths longward of 150 nm. Since the UVS solar occultation measurements are planning guidelines and not tied to mission Level 1 requirements (Pappalardo et al. 2024, this collection), this slight degradation in measured versus expected performance is acceptable (the SP was on the instrument descope list). The SP measured effective area in Fig. 17e shows a sizeable deviation from predicted efficiencies, much more than the detector QE alone could explain. The in-flight calibration of the SP is needed to determine the performance more accurately however, since systematic uncertainties from the UV-RCF ground-calibration facility alignment with the small 0.25 mm diameter aperture and a lack of pick-off mirror reflectance measurements at the 45° use angle could explain much of the discrepancy.

4.1.3 Spectral and Spatial Resolutions

Emission line spectra obtained at different spatial locations were mapped as shown in Fig. 18. These calibrations were used to assign the spatial and spectral resolutions as a function of detector location shown in Fig. 19–21, using the full-width half maximum (FWHM) of the line-spread-functions for each 0.5°. The center of the illuminated slit image maps to rows below the center of the active area of the detector, with rows above the slit image available for simultaneously determining background noise and stray-light levels.

4.1.4 Darks and Detector Linearity

A series of long dark observations were taken over multiple days and times throughout the ground-calibration campaign for a total of ~20 hours of dark acquisitions. Of these 20 hours, the first four had a cold cathode gauge operating near the instrument. Since the MCP detector is sensitive to ions, the dark background level was increased ~1 Hz higher than measurements with the gauge off. Excluding these data from the analysis, we use the remaining ~16 cumulative hours of dark images for further analysis. The detector was operated at -3550 V (the nominal HV level for room temperature at delivery) for the dark

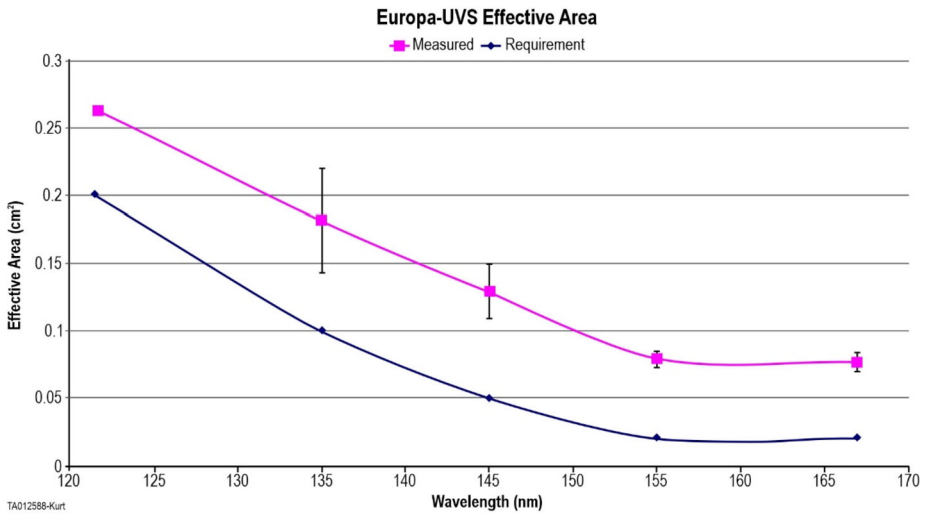


Fig. 15 The measured effective area (magenta squares) and goal (blue diamonds) for the airglow port mode plotted versus wavelength

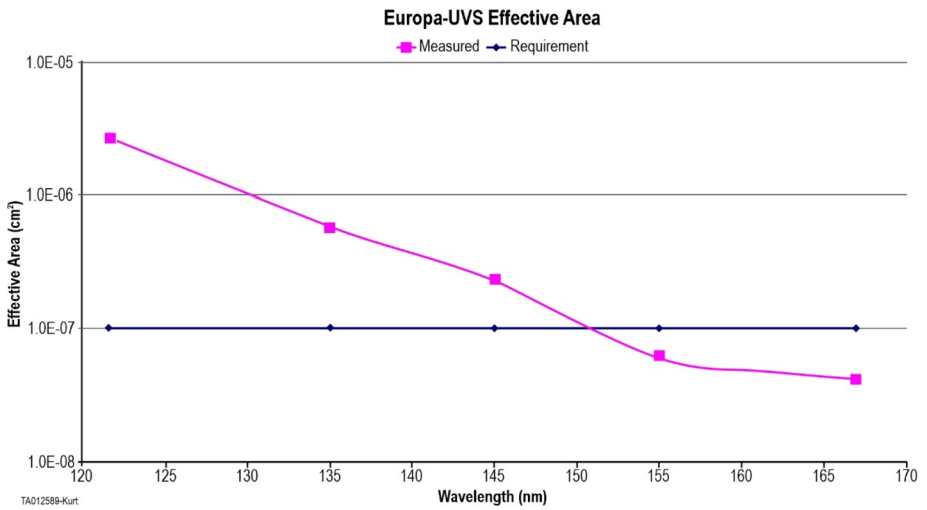


Fig. 16 The measured effective area for the solar port as a function of wavelength

measurements. All chamber windows are covered with foil to minimize any stray light in the calibration chamber. Chamber pressures were well below 8×10^{-6} Torr for all dark measurements.

Figure 22 shows the combined 16.7-hour dark image. The “warm” spots at both upper left and bottom right corners of the active area were also seen in a standalone detector dark test dataset, prior to instrument assembly. The small “hot” spot in the lower center of the active area is also still present, albeit at a much lower intensity. The overall dark rate is lower than that measured during standalone detector testing due to a lower ambient pressure

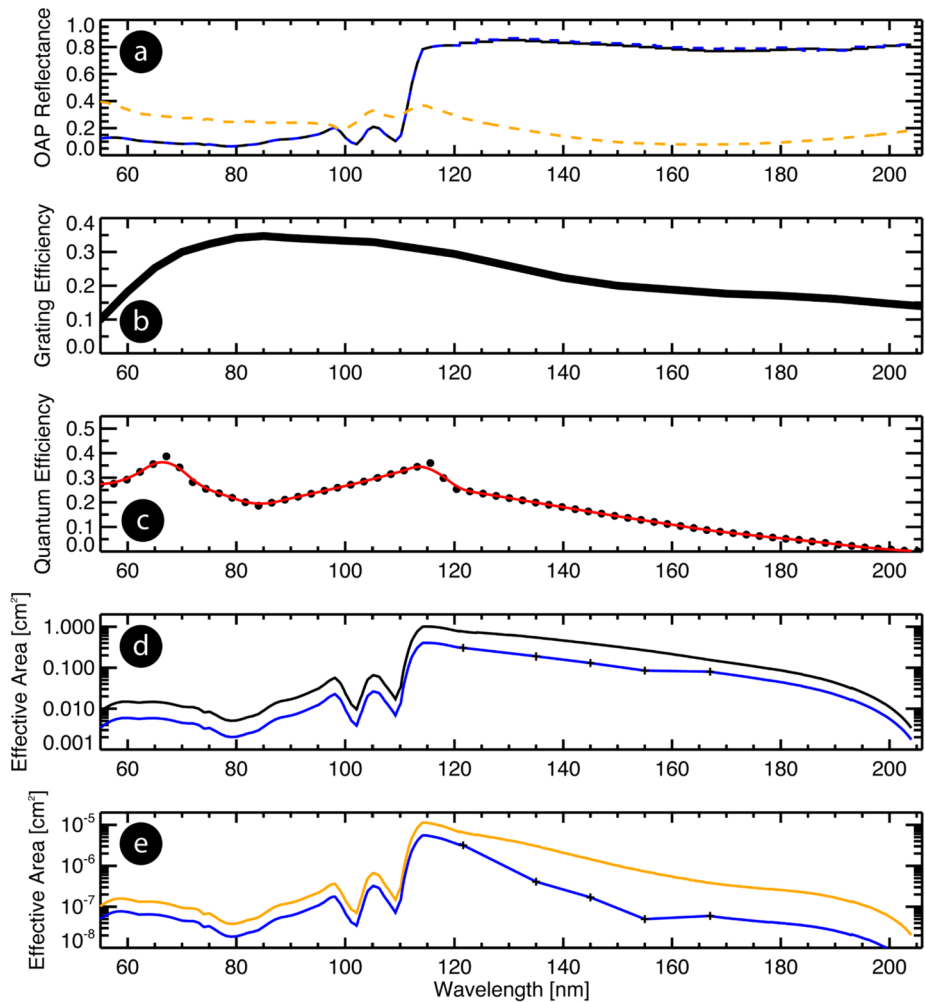


Fig. 17 Final best estimate of pre-launch effective area performance based on an optical performance model of more detailed spectral variations in effective area scaled to match the measured points in Fig. 15 (airglow port) and Fig. 16 (solar port). Panel a: OAP mirror reflectance (solid black), grating reflectance (dashed blue), and solar port mirror reflectance (orange). Panel b: theoretical grating efficiency. Panel c: quantum efficiency. Panel d: predicted AP effective area (black) vs measured one (blue). Panel e: predicted SP effective area (orange) vs measured one (blue)

within the detector in the calibration chamber, versus the ground support equipment (GSE) pump station with a KF-16 port pumping on the otherwise sealed detector housing. The maximum accumulated counts in a single pixel were seven counts; the average pixel had no more than one count accumulated over the 16-hour exposure.

4.1.5 Detector Dead-Times

The measured count rates by Europa-UVS, both analog and digital, are subject to dead-time effects, which decreases the measured signal at large global or local count rates. The

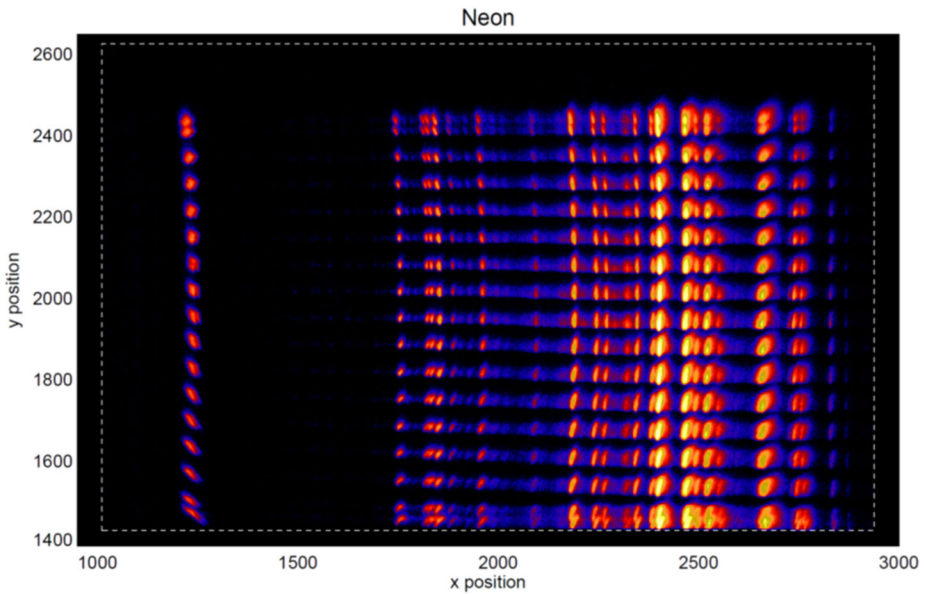


Fig. 18 A composite of Ne emission measured at $\sim 0.5^\circ$ offset angles in y-position through the Europa-UVS HP aperture. The derived spectral and spatial resolutions (Figs. 19 to 21) are based on these types of calibration data

characteristic dead time for the digital count rate is higher due to the additional processing required by the electronics. Pre-launch measurement of the characteristic dead times allow us to correct the count rates using:

$$D_{corr} = \frac{D}{1 - D\tau_D}, \tag{3}$$

where D and D_{corr} are the digital and corrected digital count rate, respectively, and τ_D is the digital count rate. As Davis et al. (2021) report, $\tau_D = 825$ ns for Europa-UVS. This results in a 10% loss of recorded events for the digital count rate at an input rate of 110 kHz. A 1% uncertainty in τ_D would propagate to a 1.1% systematic uncertainty in D_{corr} and a 9.87% to 10.09% loss range at 110 kHz in this example.

Analog and digital global count-rate limits: Based on the analog (raw) and digital (event) dead-time values, the reported count rates (analog) and captured science data (event) are lower than the true rates. With an analog count rate assuming a dead time of 150 ns ($A = R/(1+R\cdot\tau_{analog})$), the maximum count-rate asymptotes at 6.67 MHz. With a digital count rate assuming a dead time of 825 ns ($D = R/(1+R\cdot\tau_{digital})$), maximum count-rate asymptotes at 1.21 MHz.

Local “gain-droop”: A local gain degradation also occurs when an especially bright point source or emission line feature draws charge from a microchannel plate pore faster than the charge can be replenished per its local RC time constant, resulting in fewer photo-electrons collected and therefore a lower measured local count rate (Ertley et al. 2017). The correction for this effect, if any, awaits analysis of in-flight calibration data. For example, observations viewing the same bright targets with both the AP and HP apertures provide useful ratio methods to characterize the local gain-droop.

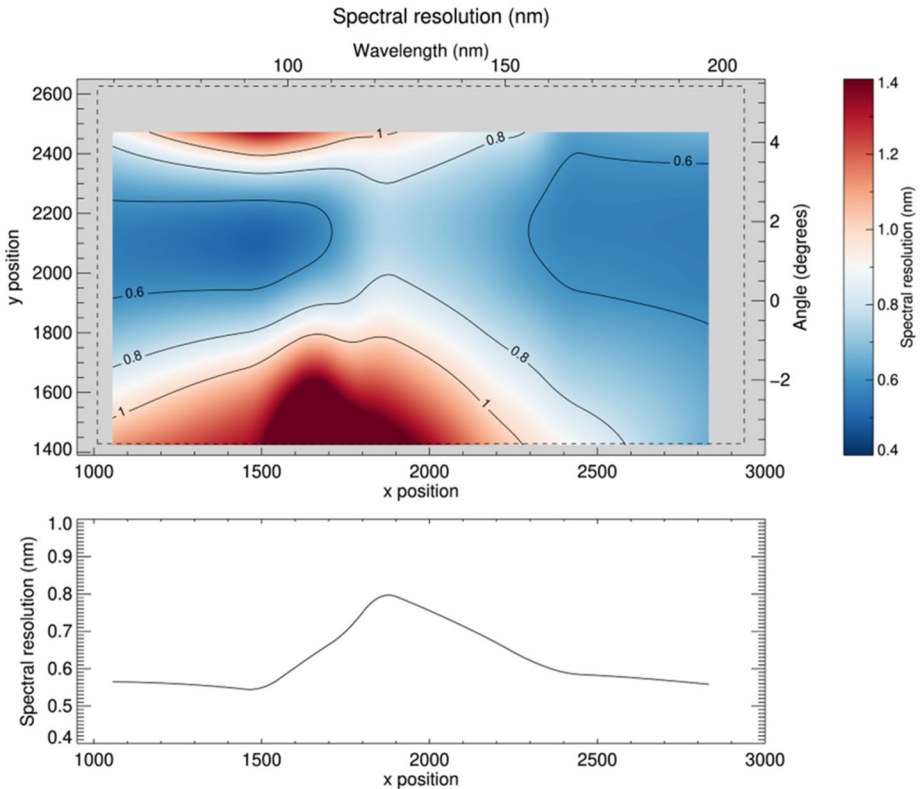


Fig. 19 (top) A colored plot of spectral resolution versus x and y position on the detector. Wavelength is labeled on the upper axis, and relative off-axis angle on the right axis. (bottom) All on-axis positions have better than 1-nm spectral resolution

4.1.6 Stray-Light

Europa-UVS’s stray-light rejection was characterized along both spectral and spatial axes at the UV-RCF (Fig. 23). The test procedure involved illuminating the airglow entrance aperture with a collimated beam reflected by the OAP mirror at various off-axis angles. We performed the scattered-light analysis at Lyman- α because it is the brightest UV emission line in both the hollow cathode lamp spectrum and the solar spectrum.

The motorized stage supporting Europa-UVS enabled us to swivel the AP view between -12° to $+12^\circ$ in the spectral plane (perpendicular to the slit length, while keeping the spatial axis fixed at the slit center). Similarly, the spectrograph was also tilted in the spatial plane from -11° to $+11^\circ$ (parallel to the slit length, while maintaining the spectral axis at slit center).

The acquired images by the MCP detector were analyzed to determine the point-source-transmittance (PST) as a function of angular offset from the Europa-UVS airglow boresight axis. PST is the ratio of stray-light irradiance E_{FP} on a MCP detector at the Europa-UVS focal plane to source irradiance at the instrument aperture E_{input} . This expression (eqn. (4) can be rewritten in terms of the measured off-/on-axes count-rate ratio (R_{off}/R_{on}), the Lyman- α effective area ($A_{eff-Ly\alpha}$), the focal plane active area (A_{FP}), quantum efficiency (QE) of the

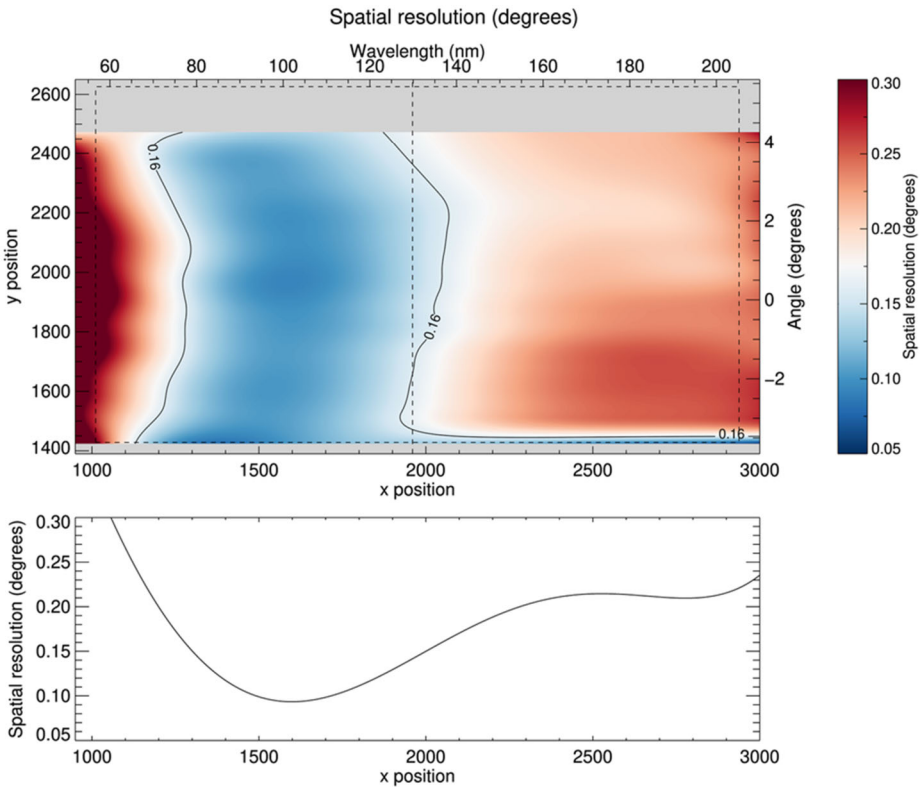


Fig. 20 (top) The spatial PSF FWHM as a function of wavelength and relative off-axis angle measured through the AP. (bottom) The spatial PSF FWHM near the center of the slit

detector at Lyman- α , and the geometric ratio of the beam size A_b to the size of the entrance aperture A_g .

$$PST = \left(\frac{A_{eff-Ly\alpha}}{QE A_{FP}} \right) \left(\frac{A_b}{A_g} \right) \left(\frac{R_{off}}{R_{on}} \right) \tag{4}$$

The Lyman- α effective area and QE values used to compute the PST were measured during instrument radiometric and detector vendor tests ($A_{eff-Ly\alpha} = 0.26 \text{ cm}^2$; $QE = 0.25$; $A_b / A_g = 0.25$; $A_{FP} = 7.5 \text{ cm}^2$). With these input values, we estimate a PST of 0.035 at the on-axis position, aligned to the airglow boresight. The requirement of $PST < 10^{-6}$ at off-axis angles $> 7^\circ$ was met in both axes.

4.2 In-Flight Calibration Plans

After launch, Europa-UVS undergoes several commissioning activities before conducting routine calibrations during cruise phase, more prior to Jupiter orbit insertion (JOI), and repetitively during the science tour phase. All of the performance properties described for the ground calibration are reanalyzed and in almost all cases determined more precisely with the in-flight data calibrations.

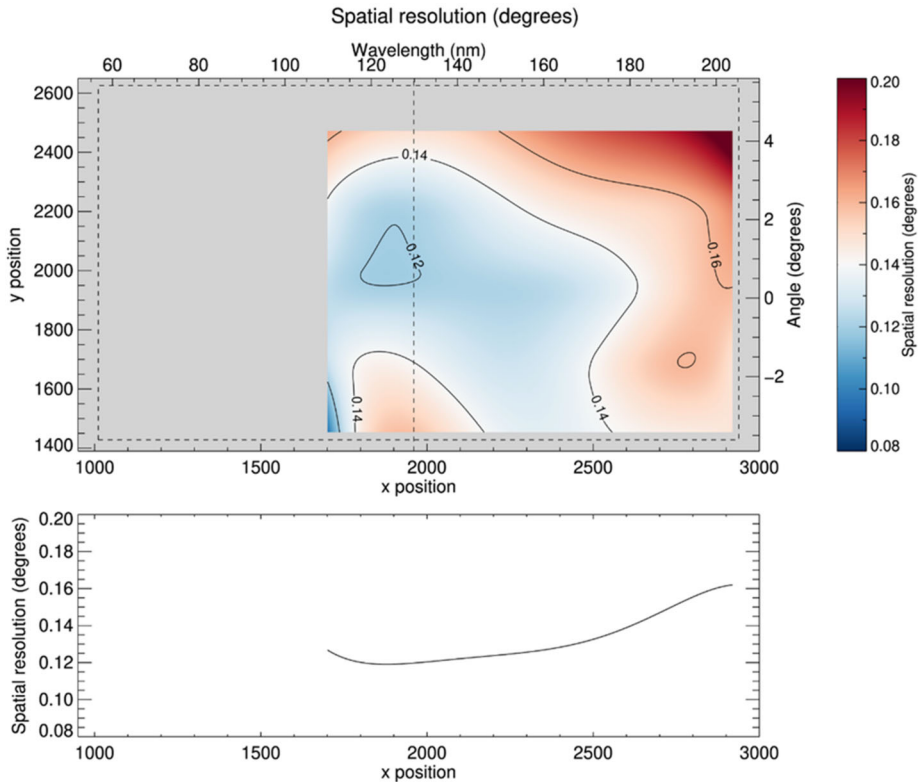


Fig. 21 (top) The spatial PSF FWHM as a function of wavelength and relative off-axis angle measured through the HP. (bottom) HP spatial resolution versus x position near the center of the slit

The initial commissioning of the instrument involves different phases of powering the LVPS to turn on the instrument, performing electrical functional tests, actuating the launch latches to release and open the aperture doors, followed by opening of the detector door with its one-time actuated wax pellet mechanism, ramping up the HVPS for the first time, and characterizing the detector dark signals. The dark observation is planned for 24-hours to check for hotspots and other irregularities that may have occurred since the previous calibration. These occur yearly during cruise. Since the spacecraft pointing during inner cruise is constrained thermally, the “first-light” spectrum is obtained opportunistically with sky Lyman- α and HeI 58.4 nm emissions filling the slit as an extended source and with whatever stellar sources might be in the field (if any). Another acquisition during a roll slew is planned to ensure stellar sources are also obtained. Several months later at a further distance to the Sun dedicated star pointings, raster scans, nods along the slit, and other calibrations are completed with both AP and HP modes.

During cruise, UVS performs point and stare star “step-scan” observations of a star at ~ 14 independent positions along the 7.5° slit at 0.5° offsets with a once per year cadence. These observations determine the Europa-UVS wavelength calibration, point spread function (PSF) as a function of wavelength, the spatial plate scale, and the effective area at wavelengths longer than 121.6 nm. The observations at multiple slit positions measure these quantities with respect to observed spatial position and give a rough value for the flat field.



Fig. 22 Image histogram of the dark pixellist exposures for 16.7 hours of accumulated exposure. The color bar represents total counts in a given pixel over the accumulated exposure

Once the spacecraft is >2 AU from the Sun at a location where the global count rates would not be exceeded, the SP is pointed to the Sun and calibrated through a five-minute stare. Bright stars are also observed in the SP for 30-minutes and compared with a five-minute stare of the same bright star through the HP to calibrate between the FOVs.

Pre-JOI campaigns observe the EUV/FUV emission from the Io plasma torus simultaneously with the FUV emissions from Jupiter's aurora in order to further calibrate the instrument at EUV wavelengths, which cannot be calibrated with stars due to interstellar absorption <91.2 nm. Similar to the Europa neutral cloud and torus dataset, these observations spatially map the extent of neutral and ionized gas signals throughout the satellite orbital plane ranging from one extreme location for Europa to the other. The signals from the Io plasma torus are much brighter and more suitable for this calibration purpose.

Throughout the tour phase of the mission, most of the in-flight calibrations that occurred during cruise are repeated; some occur repeatedly with each orbit of Jupiter, while others are conducted on a yearly basis, as follows. During each orbit, a dark observation near apojove is planned to check for any new hotspots or changes to the detector since the previous calibration. This observation is similar to the dark observations conducted during cruise, but shorter, at ~ 1 hour. A radiation observation (Sect. 3.7.7) is conducted twice per flyby: prior to the first scan in approach and following the last scan in departure. The duration of these calibrations is one hour each.

The sensitivity of the instrument is tracked, in part, by observing the brightness of the stars used for the stellar occultation observations (Sect. 3.7.3). However, for orbits that do not include a stellar occultation, Europa-UVS conducts shorter, ten-minute versions of the star stare nods in both AP and HP mode (Sect. 4.2). The one-hour long star stare nods are conducted once per year in AP mode and once per year in HP mode. Sun stares through the SP are conducted in pixellist mode approximately yearly, and in histogram mode quarterly

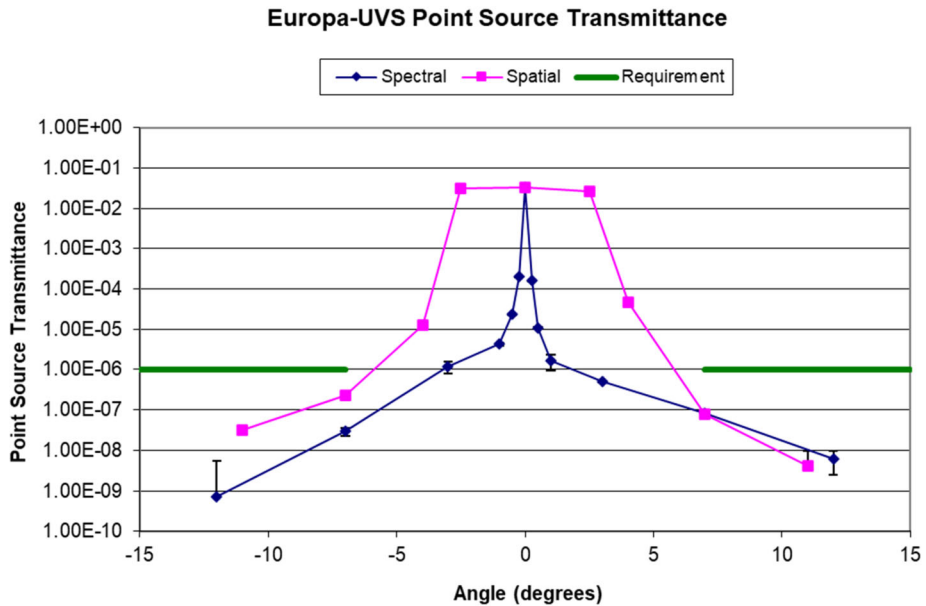


Fig. 23 The measured stray-light rejection as a function of the input off-axis angle with respect to the bore-sight in both axes. Both the spectral data values (blue squares) and the spatial values (magenta squares) are shown along with the specification requirement (green line), which was achieved

to obtain direct measurements of the solar flux at Europa as a divisor and therefore calibrate the spectral albedo datasets, provided the time and resources are available to the spacecraft.

A full-slit raster scan, which consists of a series of 2° across-slit slews past a star at locations along the slit spaced by 0.5° apart, is conducted once following JOI, within one month of the science phase. These measurements ensure the overall alignment and sensitivity of the Europa-UVS FOV has not changed. One across-slit raster, which slews the spacecraft such that a star crosses the UVS FOV in three locations along the slit, and one along-slit raster, which slews the spacecraft such that a star is tracked along the 7.5° slit in three locations parallel to the slit, as well as one star-step scan, are also conducted annually following JOI.

The line spread function across the UV bandpass is calibrated once post-JOI in AP mode and one time in HP mode through extended source calibrations. The extended source can be either Jupiter or other large bodies in the system, such as Jupiter's satellites. These are necessary because the line spread function is different for a point-source like a star vs. an extended object that exceeds the size of a resolution element.

The EUV/FUV calibration that began with Io plasma torus or any opportunistic planetary targets pre-JOI continues post-JOI approximately annually. These pointed Io Torus, satellite, and/or Jupiter observations consist of consecutive acquisitions for week-long periods, as available, and tailored to available downlink. They continue to monitor changes to the instrument sensitivity at EUV wavelengths.

5 Instrument Operations Planning

The Europa Clipper project science planning process is described in Pappalardo et al. 2024, this collection. The project provides the instrument operations team an initial sequence of

Europa-UVS activities that adhere to scheduling rules provided for each payload activity, in accordance with the project's templated repeatable science observation strategy. These activities, however, have a default set of LUTs-defining parameters such as the spatial, spectral, and sampling time resolution for the observations that the Europa-UVS team can choose to update in an iterative process with the project. An online planning tool developed for Europa-UVS ingests Europa Clipper's activity sequence for each flyby, placing those activities on an interactive timeline for edits to these preset LUT and related parameters as needed. Along with basic geometric information such as altitude and phase angle, the Europa-UVS online tool provides a sequence of images to show the overall perspective of the spacecraft and Europa during the flyby. It also calculates in real-time the anticipated data volume produced by the sequence of activities.

Requested edits to the flyby sequence investigated within the webtool can include adjusting the timing and length of the observations. Each defined activity can also be directly edited to change the LUTs to optimize the detector parameters for each observation. Editing the activity itself is done in a separate, connected webtool that can implement interactive decisions for the spectral and spatial dimensions. This observation-card designing tool can then be used to estimate the expected SNR across the detector, accounting for background radiation and other parameters.

As described in Sect. 3.7.3, the stellar occultation prioritization scheme we plan is semi-automated, with available stellar occultation events given an initial adjectival priority ranking automatically. The Europa-UVS team may increase or decrease the relative ranking of schedulable events based on these example criteria as first reported in Velez et al. 2024: 1) Fills global location and time coverage needs; 2) Passes through candidate plume locations; 3) Previously observed with Europa-UVS; 4) Has IUE or other known spectra, not only models; 5) Low flux variability and/or high accuracy of parameters such as astrometry; 6) Emphasizes extreme-UV (<115 nm) capability and sensitivity to additional species; 7) Pair of events, two chords at once (lines connecting ingress and egress for astrometric calculations), or proximity to another UV-bright star; 8) Times when background radiation levels near the spacecraft are low; 9) Follows the Clipper trajectory line of sight for best in-situ (MASPEX + SUDA) comparisons; 10) Lines up with radar (REASON) ground-track for best astrometry correlation; 11) Coincides with images (EIS) of high phase limb plume search locations; 12) Relatively less auroral brightness, impacting cases with borderline SNR; 13) Near-simultaneity with JUICE encounters; 14) Near-simultaneity with JUICE-UVS occultation observations; and 15) Avoids scheduling conflicts with other key observations or mission events.

Once all activities have been investigated by the Europa-UVS team and edited as needed, the tool can then produce two files: one that can be sent to the Europa Clipper project to indicate the requested changes to the sequence by the Europa-UVS team (both pointing and non-pointing related); and the sequential information needed to generate the command load for Europa-UVS. These products are used when communicating with the project Thematic Working Groups, Strategic Science Group, and Tactical Science Group personnel for final sequence-related decisions (Pappalardo et al. 2024, this collection).

6 Data Processing and Products

6.1 Instrument Science Operations Center (ISOC)

The Europa-UVS instrument Science Operations Center (iSOC) produces data products (raw and calibrated) that are delivered to NASA's Planetary Data System (PDS) for distribu-

tion to the public and archiving. The Europa-UVS iSOC pipeline consists of two sequential elements, named “Lima” and “Mike”. First, “Lima” converts the telemetry data files into raw data products, and then “Mike” calibrates and spatially locates the data contained in the raw data products, resulting in the calibrated data products.

A Europa-UVS iSOC pipeline “executive” program checks for newly delivered data files on a periodic basis. The periodicity of this program can be set based on operational needs. After cataloging the received files, the “executive” program initiates the Europa-UVS SOC data processing pipeline. The first element of the pipeline (“Lima”) converts the raw data files into raw data products (PDS4 Raw). These products represent the lowest processing level of the Europa-UVS data and are delivered to the PDS. No calibrations are applied to the science data at this stage. Raw telemetry values are converted to engineering units where applicable; however, both raw and converted values are included in the raw data product. Multiple versions of the output raw products are made available if software bugs affecting the output data are uncovered and corrected. In the event of an error whose correction alters released data, the data are reprocessed by the revised software and then delivered to the PDS. The second element of the pipeline (“Mike”) calibrates and spatially locates the data contained in the raw data products, resulting in the calibrated data products (PDS4 Calibrated). As with the raw files, the calibrated files are delivered to the PDS.

6.2 Lower-Level Items and Formats

The Europa-UVS PDS4 raw data product (created from instrument telemetry packets) contains data from histogram and pixellist science packets, as well as count-rate, housekeeping, and memory-dump packets. One file is produced per instrument turn-on. The raw data products are stored using the Flexible Image Transport System (FITS) file format, useful for multi-dimensional array table-based formats (i.e., one “extension” per table within the same file). A Europa-UVS PDS4 raw data file includes the following extensions:

Spectral Summary Image: This image summarizes the spectral data captured for all exposures included in the file for both histogram and pixellist modes.

Spatial Summary Image: This image summarizes the spatial data captured for all exposures included in the file for both histogram and pixellist modes.

Acquisition List: This dataset uses the histogram, pixellist, and housekeeping data to build a list of expected observations. Each acquisition may use distinct configuration items such as LUTs and masking definitions, which are listed here.

LUT Definition: This extension provides the definitions of the Lookup Tables (LUTs) used during science acquisitions.

Mask Definition: This extension provides the specification of each of the ten masking slots used by a given acquisition.

Frame List: This dataset contains a list of the generated frames for both histogram and pixellist data. The packets of each acquisition are organized into one or more transfer frames for downlink. This extension summarizes information at the frame level.

Raw Packet Data: This dataset contains all of the raw data from the science frame, with the packet header data removed.

Engineering Count-Rate Product List: This extension contains a table of count-rate data products. In this extension the counts have been converted to frequency based on the sample period.

Raw Count-Rate Packet Data: This dataset contains all of the raw data from the count-rate packets. In this extension the counts are presented in a raw form, exactly as recorded in the packet.

Count-Rate Band Definitions: The count rates are integrated over bands (ranges of pixel columns). For each band definition this extension lists the time the definition becomes active along with the high and low column numbers that define the band.

Raw Housekeeping Data: This dataset contains the complete housekeeping dataset in a raw format.

Engineering Housekeeping Data: This dataset contains the complete housekeeping dataset in calibrated engineering units, where applicable.

Parameter List: This table records the known values of the instrument parameter table, an internal configuration table whose contents are reported as part of the housekeeping packet.

Memory-Dump Data: This extension contains raw memory-dump packets, if any are commanded during the powered-on time range covered by the FITS file.

Science Metadata: This dataset contains the complete set of Accountable Data Product (ADP) metadata packets that are transmitted before and after each acquisition. These metadata packets are produced before and after each acquisition to provide traceability information on the time range and number of packets produced within the context of Europa Clipper's data handling approach.

Acquisition Data: Most importantly, the final set of FITS file extensions contain the data collected for each histogram and pixellist acquisition. For each pixellist acquisition a table is created to list the recorded photons. For each histogram acquisition two image extensions are created, one for the array-totaled histogram image and one for the pulse height distribution during the integration time interval. Many such extensions are included in a typical file to include the full sequence of observations planned, and these include the primary science information for the data user.

The calibrated data products are similarly FITS files with several extensions preceding the acquisition data extensions. Summary image extensions are in calibrated formats, and a spatially mapped wavelength calibration image is included using an average for the duration of the acquisitions in that file. Relevant geometry information is also included in the calibrated data products, including several coordinate frames such as planetographic latitude and longitude, sky right-ascension and declination, moon-nearest-point altitudes, and so on. See the software interface specification document in the Planetary Data System for the detailed definitions for each calibrated data product extension, currently under development.

6.3 Higher-Level Data Products

Each of the science activities described in Sect. 3.7 contributes to higher-level data products. Aurora and airglow spectral images and spectrograms are produced from the dedicated Europa SAA stares and the Europa scans. From these raw data products, two types of maps are produced: (1) UV auroral-brightness maps at a few wavelengths of interest; and (2) surface-brightness maps at a few wavelengths of interest. These maps can be made from both dayside and nightside observations of Europa.

The observed morphology and brightness of the UV emissions in the auroral-brightness maps, and how they change with time, are connected to the properties of the magnetospheric environment and can be used to constrain how Europa's atmosphere interacts with the local plasma environment (e.g., Roth et al. 2016). Comparative maps between key wavelengths such as oxygen and hydrogen can be used to search for plumes; Roth et al. (2014a, 2014b) identified the first putative plume on Europa through the persistent detection of coincident hydrogen and oxygen UV emissions at the appropriate relative abundance ratio for dissociated water. Atmospheric abundances are determined from the auroral-brightness maps, with knowledge of Europa's position in Jupiter System III coordinates. The derivation of

the abundances constrains the exchange of material between Europa's surface with its atmosphere, and Europa's atmosphere with the local space environment (including material originating from Io). Changes in the relative abundances of the atmospheric constituents can be used to trace how Europa's atmosphere responds to daily temperature variations and should reflect sporadic events including plume injections into the atmosphere.

The surface-brightness maps enable assessment of properties across Europa's surface, including grain size and composition. Near-global surface-ratio maps of UV off-band (155–190 nm) to on-band (130–155 nm) albedos, similar to those produced by LAMP (e.g., Byron et al. 2021; Magaña et al. 2022), can be used to map relative surface maturity. Maps of the spatial distribution of Lyman- α (121.6 nm) reflectance, which currently appears to be roughly inverted in brightness from visible maps (McGrath et al. 2009; Roth et al. 2014a,b), can be compared with global and regional images from EIS and MISE to further explore surface composition, maturity, and other regolith properties. The UV maps can also be correlated with identified geologic regions of interest for indications of unique surface properties in those regions. Comparative maps near the 165-nm water ice spectral edge (e.g., on-band, edge, and off-band as defined in Hendrix et al. 2019) can also be used to identify fresh deposits of water that would stand out against the rest of the irradiated, UV-darkened surface (e.g., Becker et al. 2018; Raut et al. 2023). Spectral-albedo image cubes at 2–10-nm resolution and spectral-slope map products are also envisioned. As with LAMP observations (Gladstone et al. 2012), nightside surface-reflectance maps could be made using ambient starlight, interplanetary medium skyglow, and Jupitershine, which could be most useful if there are permanently shadowed regions found near Europa's poles.

To constrain surface composition using the surface reflectance spectra, continuing laboratory studies of the far-UV reflectance of water ice, mixtures, and irradiated samples are planned. The low albedo of Europa's surface reported by Becker et al. (2018) using HST observations presents an interesting problem since water ice-rich surfaces are expected to be bright longward of the absorption edge at 165 nm. Could the presence of trace constituents like CO₂, SO₂ and their irradiated byproducts serve to darken Europa's surface? Planned experiments will characterize the FUV darkening of Europa-ice analogs processed by energetic irradiation. Similar studies previously constrained the single scattering albedo and scattering anisotropy in light reflected by the canonical Apollo 10084 soil and lunar simulants, as demonstrated in Raut et al. (2018b) and Gimar et al. (2022). These results were valuable in the interpretation of LRO-LAMP datasets.

Raw stellar occultation profiles of signal vs. time are converted to transmission profiles as a function of altitude above the surface for another type of higher-level product. Each transmission profile provides a high-resolution probe of the relative amount of absorption by the slice of Europa's atmosphere that occulted the star. Compositional abundances can then be determined from these transmission profiles, and the overall structure of the atmosphere can be explored by assessing these transmission profiles at different altitudes above the surface. Because the stellar occultations are expected to occur over the duration of the mission and through different regions of the atmosphere, comparisons between the profiles serve to explore local variability and long-term changes in the composition and structure of the atmosphere.

Jupiter transit observations result in a global view of Europa while backlit by Jupiter. From these raw observations, atmospheric-absorption profiles of Europa at Lyman- α (121.6 nm) are derived. The absorption profiles from this silhouette are then used to observe the extent of Europa's atmosphere above its limb and search for current activity such as plumes. Lyman- α is the brightest wavelength reflected from Jupiter and therefore the wavelength with the highest SNR, better enabling the detection of absorptions by Europa's atmosphere and a water vapor plume (if present).

The torus and neutral cloud stares each result in a number of spectral images of the Europa torus and neutral clouds that may exist near Europa's orbit. Emissions detected within the acquired spectral images are used to produce a higher-level data product of compositional abundances and the overall extent of the torus and/or neutral clouds. These data are reflective of the rate of loss of material from Europa into the local space environment, either via sputtering of the surface, ionization of the atmosphere, or possibly directly from ongoing activity such as plumes.

6.4 Quick-Look and Collaborative Data Products

To facilitate quality checks and provide information for providing tactical changes to observation plans several data products are generated quickly upon receipt of the data at the iSOC. These "quick-look products" are immediately useful for collaborative science purposes, with the caveat that more accurate or detailed higher-level products more suitable for science publications will eventually be available. The lower-level count-rate product list, raw count-rate packet data, and its corresponding count-rate band definition (see Sect. 6.2) are a primary tool for validating the performance of Europa-UVS during acquisitions at glance. These three higher level quick-look products will be of more interest to a general scientist: 1) preliminary full-disk maps and pushbroom observations, 2) preliminary surface brightness maps, and 3) transmission profiles with wavelength for candidate plume search locations. Lastly, a map of surface composition for features of interest will prove useful for collaborative overlays with the other remote sensing datasets, and are iteratively improved throughout the mission.

6.5 Housekeeping and Engineering Data Products

Europa-UVS's housekeeping data stream is transmitted to two destinations on the spacecraft: one to the spacecraft computer directly and one to the Bulk Data Storage (BDS) recorder. This telemetry is sent to both destinations at a nominal 1 Hz rate. Europa-UVS tracks the number of detected photon events at configurable rates and these count rate products are also sent with the housekeeping telemetry (Sect. 3.5). The digital counters are distinguished by different onboard processing levels and five parallel counters for configurable spectral bands. These count rates are transmitted to the ground in Europa-UVS count-rate science packets, then incorporated into archival data products. The BDS-recorded housekeeping is kept intact as a whole packet, ensuring sampling continuity throughout all fields.

6.6 Archiving

Data products produced by the Europa-UVS iSOC are archived in NASA's PDS for long-term access. Data are archived according to the PDS4 standard and the Europa Clipper Science Data Management Plan.

The Europa Clipper Mission Operations System (MOS) delivers spacecraft telemetry data packets to the Europa-UVS iSOC. The iSOC is then responsible for processing the telemetry into PDS4 raw, calibrated, and derived archive data products. In addition to the FITS files containing the data products, the iSOC also produces extensible markup language (XML) label files in accordance with the PDS4 standard, along with accompanying documentation and ancillary information files. These are then assembled into archive bundles and submitted to PDS for long-term archival storage.

Peer reviews of sample data products are organized throughout the life of the mission. Europa-UVS raw data products are peer reviewed before launch, with another peer review scheduled late in the cruise phase for calibrated data products.

Archiving activities are organized through periodic meetings of Europa Clipper's Data and Archive Working Group (DAWG). The DAWG consists of representatives from each investigation team, along with project and PDS personnel.

7 Summary

Europa Clipper's ultraviolet instrument, Europa-UVS, is designed to investigate key questions informing Europa's potentially habitable environment. Europa-UVS is ready to 1) search for and characterize any current activity as indicated by vapor plumes; and to 2) characterize the composition and sources of volatiles sufficient to identify the signatures of non-ice materials, including organic compounds, in globally distributed regions of the atmosphere and local space environment. The Europa-UVS design is based on the JUICE-UVS instrument, launched first and now successfully operating; they are planned to join each other during their tours at Jupiter starting in 2030 and 2031, respectively. Both UVS instruments have broader wavelength coverage, lower radiation noise susceptibility at Jupiter, improved dynamic range in count-rate and gain stability with fluence, and up to ten times better spatial resolution at certain wavelengths than predecessor UVS/Alice spectrographs. With repeatable sequences of nadir-pointed and off-nadir pointed observation activity types, the data sets expected from Europa-UVS are destined to lead to many unexpected discoveries while completing the main mission objectives.

Acknowledgements This work was supported by NASA through the Europa Clipper Project. VH acknowledges support from the French government under the France 2030 investment plan, as part of the Initiative d'Excellence d'Aix-Marseille Université – A*MIDEX AMX-22-CPJ-04.

Declarations

Competing Interests This work was financially supported by NASA through the Europa Clipper project.

Open Access This article is licensed under a Creative Commons Attribution 4.0 International License, which permits use, sharing, adaptation, distribution and reproduction in any medium or format, as long as you give appropriate credit to the original author(s) and the source, provide a link to the Creative Commons licence, and indicate if changes were made. The images or other third party material in this article are included in the article's Creative Commons licence, unless indicated otherwise in a credit line to the material. If material is not included in the article's Creative Commons licence and your intended use is not permitted by statutory regulation or exceeds the permitted use, you will need to obtain permission directly from the copyright holder. To view a copy of this licence, visit <http://creativecommons.org/licenses/by/4.0/>.

References

- Abrahams JNH, Nimmo F, Becker T, Gladstone R, Retherford KD, Steinbrugge G, Mazarico E (2021) Improved determination of Europa's long-wavelength topography using stellar occultations. *Earth Space Sci* 8:e2020EA001586. <https://doi.org/10.1029/2020EA001586>
- Araki H, Tazawa S, Noda H, Ishihara Y, Goossens S, Sasaki S, et al (2009) Lunar global shape and polar topography derived from Kaguya-LALT laser altimetry. *Science* 323(5916):897–900. <https://doi.org/10.1126/science.1164146>
- Bagenal F, Dols V (2020) The space environment of Io and Europa. *J Geophys Res Space Phys* 125:e2019JA027485. <https://doi.org/10.1029/2019JA027485>

- Becker TM, Retherford KD, Roth L, Hendrix AR, McGrath MA, Saur J (2018) The far-UV albedo of Europa from HST observations. *J Geophys Res, Planets* 123:1327–1342. <https://doi.org/10.1029/2018JE005570>
- Becker TM, Trumbo SK, Molyneux PM, Retherford KD, Hendrix AR, Roth L, Raut U, Alday J, McGrath MA (2022) Mid-ultraviolet Hubble observations of Europa and the global surface distribution of SO₂. *Planet Sci J* 3:129. <https://doi.org/10.3847/PSJ/ac69eb>
- Becker TM, Zolotov M, Gudipati MS, et al (2024) Exploring the composition of Europa with the upcoming Europa Clipper Mission. *Space Sci Rev* 220:49. <https://doi.org/10.1007/s11214-024-01069-y>
- Blaney DL, Hibbitts K, Diniega S, et al (2024) The mapping imaging spectrometer for Europa. *Space Sci Rev* 220:80. <https://doi.org/10.1007/s11214-024-01097-8>
- Blankenship DD, Moussessian A, Chapin E, et al (2024) Radar for Europa assessment and sounding: ocean to near-surface (REASON). *Space Sci Rev* 220:51. <https://doi.org/10.1007/s11214-024-01072-3>
- Blöcker A, Saur J, Roth L (2016) Europa's plasma interaction with an inhomogeneous atmosphere: development of Alfvén winglets within the Alfvén wings. *J Geophys Res Space Phys* 121:9794–9828. <https://doi.org/10.1002/2016JA022479>
- Byron BD, Retherford KD, Czajka E, Cahill JTS, Hendrix AR, Greathouse TK (2021) Lunar surface composition constraints from maturity-corrected far-ultraviolet reflectance maps. *Planet Sci J* 2:189. <https://doi.org/10.3847/PSJ/ac1d53>
- Carlson RW, Calvin WM, Dalton JB, Hansen GB, Hudson RL, Johnson RE, McCord TB, Moore MH (2009) Europa's surface composition. In: Pappalardo RT, McKinnon WB, Khurana KK (eds) *Europa*. University of Arizona Press, Tucson, pp 283–327
- Castelli F, Kurucz RL (2003) New grids of ATLAS9 model atmospheres. *IAU Symp* 210:A20. <https://doi.org/10.48550/arXiv.astro-ph/0405087>
- Castelli F, Kurucz RL (2006) Computed H-Beta indices from ATLAS9 model atmospheres. *Astron Astrophys* 454:333–340. <https://doi.org/10.1051/0004-6361:20064999>
- Christensen PR, Spencer JR, Mehall GL, et al (2024) The Europa Thermal Emission Imaging System (E-THEMIS) investigation for the Europa Clipper Mission. *Space Sci Rev* 220:38. <https://doi.org/10.1007/s11214-024-01074-s11214-024-1>
- Daubar I, Hayes AG, Collins GC, et al (2024) Planned geological investigations of the Europa Clipper Mission. *Space Sci Rev* 220:18. <https://doi.org/10.1007/s11214-023-01036-z>
- Davis MW, Greathouse TK, Gladstone GR, Retherford KD, Slater DC, Stern SA, Versteeg MH (2014) Improved ground calibration results from Southwest Research Institute Ultraviolet Radiometric Calibration facility (UV-RCF). In: *Proc SPIE 9144 Space Telescopes and Instrumentation 2014: Ultraviolet to Gamma Ray* 914433. <https://doi.org/10.1117/12.205704>
- Davis MW, Osterman SN, Gladstone GR, Retherford KD (2019) High-resolution aperture shape analysis for the JUICE and Europa ultraviolet spectrographs. In: *Proc SPIE 11118 UV, X-Ray, and Gamma-Ray Space Instrumentation for Astronomy XXI* 1111819. <https://doi.org/10.1117/12.2529668>
- Davis MW, Gladstone GR, Giles RS, Greathouse TK, Molyneux PM, Raut U, Retherford KD, Baldor S, Versteeg MH, Freeman M, Persson K, Persyn SC (2020) Ground calibration results of the JUICE ultraviolet spectrograph. In: *Proc SPIE 11444, Space Telescopes and Instrumentation 2020: Ultraviolet to Gamma Ray* 1144404. <https://doi.org/10.1117/12.2562986>
- Davis MW, Siegmund OHW, Gladstone GR, Martin A, Retherford KD, Vallerga JV (2021) TRL6 testing of a curved borosilicate glass microchannel plate far-UV detector assembly for spaceflight. In: *Proc SPIE 11821 UV, X-ray, and gamma-ray space instrumentation for astronomy XXII* 118210A. <https://doi.org/10.1117/12.2594177>
- Davis MW, Retherford KD, Molyneux PM, Gladstone GR, Eloriaga N, Giles RS, Greathouse TK, Raut U, Veach TJ, Ferrell S, Versteeg MH, Freeman MA, Persson KB (2022) Europa Clipper ultraviolet spectrograph: ground calibration results. In: *Proc. SPIE 12181 Space Telescopes and Instrumentation 2022: Ultraviolet to Gamma Ray* 1218138. <https://doi.org/10.1117/12.2630530>
- Dere KP, Landi E, Mason HE, Monsignor Fossi BC, Young PR (1997) CHIANTI an atomic database for emission lines. Paper I: wavelengths greater than 50 Å. In: *Astronomy and astrophysics. Supplement series*, vol 125, pp 149–173. <https://doi.org/10.1051/aas:1997368>
- Devaud G, Schweickart RB, Walther B, Davis MW, Raut U, Gladstone GR, Retherford KD (2018) Europa ultraviolet spectrograph: contamination transport modeling to predict mission performance. In: *Proc. SPIE 10748, systems contamination: prediction, control, and performance 2018*, 107480B. <https://doi.org/10.1117/12.2320331>
- Ermakov AI, Kreslavsky MA, Scully JE, Hughson KH, Park RS (2019) Surface roughness and gravitational slope distributions of Vesta and Ceres. *J Geophys Res, Planets* 124:14–30. <https://doi.org/10.1029/2018JE005813>
- Ertley CD, et al (2017) Microchannel plate imaging detectors for high dynamic range applications. *IEEE Trans Nucl Sci* 64:1774–1780. <https://doi.org/10.1109/TNS.2017.2652222>

- Fletcher LN, Cavalie T, Grassi D, et al (2023) Jupiter science enabled by ESA's Jupiter Icy Moons Explorer. *Space Sci Rev* 219:53. <https://doi.org/10.1007/s11214-023-00996-6>
- Fu RR, Ermakov AI, Marchi S, Castillo-Rogez JC, Raymond CA, Hager BH, et al (2017) The interior structure of Ceres as revealed by surface topography. *Earth Planet Sci Lett* 476:153–164. <https://doi.org/10.1016/j.epsl.2017.07.053>
- Gimar CJ, Raut U, Poston MJ, Stevanovic A, Protopapa S, Greathouse TK, et al (2022) Far-ultraviolet photometric characteristics of JSC-1A and LMS-1 lunar regolith simulants: comparative investigations with Apollo 10084. *J Geophys Res, Planets* 127:e2022JE007508. <https://doi.org/10.1029/2022JE007508>
- Giono G, Roth L, Ivchenko N, Saur J, Retherford K, Schlegel S, Ackland M, Strobel D (2020) An analysis of the statistics and systematics of limb anomaly detections in HST/STIS transit images of Europa. *Astron J* 159:155. <https://doi.org/10.3847/1538-3881/ab7454>
- Gladstone GR, Stern SA, Retherford KD, Black RK, Slater DC, Davis MW, Versteeg MH, Persson KB, Parker JW, Kaufmann DE, Egan AF, Greathouse TK, Feldman PD, Hurley D, Pryor WR, Hendrix AR (2010) LAMP: the Lyman alpha mapping project on NASA's lunar reconnaissance orbiter mission. *Space Sci Rev* 150:161–181
- Gladstone GR, Retherford KD, Egan AF, Kaufmann DE, Miles PF, Parker JW, Horvath D, Rojas PM, Versteeg MH, Davis MW, Greathouse TK, Slater DC, Mukherjee J, Steffl AJ, Feldman PD, Hurley DM, Pryor WR, Hendrix AR, Mazarico E, Stern SA (2012) Far-ultraviolet reflectance properties of the Moon's permanently shadowed regions. *J Geophys Res* 117:E00H04. <https://doi.org/10.1029/2011JE003913>
- Gladstone GR, Persyn SC, Eterno JS, Walther BC, Slater DC, Davis MW, et al (2017) The ultraviolet spectrograph on NASA's Juno mission. *Space Sci Rev* 213:447–473. <https://doi.org/10.1007/s11214-014-0040-z>
- Grasset O, Dougherty MK, Coustenis A, Bunce EJ, Erd C, Titov D, Blanc M, et al (2013) Jupiter ICy moons Explorer (JUICE): an ESA mission to orbit Ganymede and to characterise the Jupiter system. *Planet Space Sci* 78:1–21. <https://doi.org/10.1016/j.pss.2012.12.002>
- Grava C, Greathouse TK, Retherford KD, Davis MW, Gladstone GR, Kaufmann DE, Egan AF (2018) A method to retrieve the total flux at Lyman-alpha in microchannel plate detectors affected by gain sag: application to the LAMP UV imaging spectrograph onboard the lunar reconnaissance orbiter. *J Astron Instrum* 8(2):1950002. <https://doi.org/10.1142/S2251171719500028>
- Hall DT, Strobel DF, Feldman PD, McGrath MA, Weaver HA (1995) Detection of an oxygen atmosphere on Jupiter's moon Europa. *Nature* 373:677–679. <https://doi.org/10.1038/373677a0>
- Hansen CJ, Esposito LW, Colwell JE, Hendrix AR, Portyankina G, Stewart AIF, West RA (2020) The composition and structure of Enceladus' plume from the complete set of Cassini UVIS occultation observations. *Icarus* 344:113461. <https://doi.org/10.1016/j.icarus.2019.113461>
- Hendrix AR, Vilas F, Li J-Y (2016) The UV signature of carbon in the Solar System. *Meteorit Planet Sci* 5:105. <https://doi.org/10.1111/maps.12575>
- Hendrix AR, Hurley DM, Farrell WM, Greenhagen BT, Hayne PO, Retherford KD, et al (2019) Diurnally migrating lunar water: evidence from ultraviolet data. *Geophys Res Lett* 46:2417–2424. <https://doi.org/10.1029/2018GL081821>
- Hue V, Giles RS, Gladstone GR, Greathouse TK, Davis MW, Kammer JA, Versteeg MH (2021) Updated radiometric and wavelength calibration of the Juno ultraviolet spectrograph. *J Astron Telesc Instrum Syst* 7(04):044003. <https://doi.org/10.1117/1.JATIS.7.4.044003>
- Hue V, Cavalier T, Sinclair JA, Zhang X, Benmahi B (2024) The polar stratosphere of Jupiter. *Space Sci Rev* 220:85. <https://doi.org/10.1007/s11214-024-01119-5>
- Jia X, Kivelson MG, Khurana KK, Kurth WS (2018) Evidence of a plume on Europa from Galileo magnetic and plasma wave signatures. *Nat Astron* 2:459–464. <https://doi.org/10.1038/s41550-018-0450-z>
- Kammer JA, Hue V, Greathouse TK, Gladstone GR, Davis MW, Versteeg MH (2018) Planning operations in Jupiter's high-radiation environment: optimization strategies from Juno-UVS. In: *Proc. SPIE 10699, Space Telescopes and Instrumentation 2018: Ultraviolet to Gamma Ray* 106993A. <https://doi.org/10.1117/12.2312261>
- Kempf S, Tucker S, Altobelli N, et al (2024) SUDA: a SURface Dust Analyser for compositional mapping of the Galilean moon Europa. *Space Sci Rev* 220
- Kivelson MG, Bagenal F, Kurth WS, Neubauer FM, Paranicas C, Saur J (2004) Magnetospheric interactions with satellites. In: Bagenal F, Dowling TE, McKinnon WB (eds) *Jupiter: the planet, satellites and magnetosphere*, vol 21. Cambridge University Press, Cambridge, pp 513–536
- Kivelson MG, Jia X, Lee KA, Raymond CA, Khurana KK, et al (2023) The Europa Clipper Magnetometer. *Space Sci Rev* 219:48. <https://doi.org/10.1007/s11214-023-00989-5>
- Magaña LO, Retherford KD, Byron BD, Hendrix AR, Grava C, Mandt KE, Raut U, Czajka E, Hayne PO, Hurley DM, Gladstone GR, Poston MJ, Stickle A, Greathouse TK, Cahill JT, Pryor W (2022) LRO-LAMP survey of lunar south pole cold traps: implication for the presence of condensed H₂O. *J Geophys Res, Planets* 127:e2022JE007301. <https://doi.org/10.1029/2022JE007301>


- Mazarico E, Buccino D, Castillo-Rogez J, et al (2023) The Europa Clipper gravity and radio science investigation. *Space Sci Rev* 219:30. <https://doi.org/10.1007/s11214-023-00972-0>
- McGrath MA, Lellouch E, Strobel DF, Feldman PD, Johnson RE (2004) Satellite atmospheres. In: Bagenal F, et al (eds) *Jupiter: the planet, satellites and magnetosphere*. Cambridge Univ., Cambridge, pp 457–483
- McGrath MA, Hansen CJ, Hendrix AR (2009) Observations of Europa's tenuous atmosphere. In: Pappalardo RT, McKinnon WB, Khurana KK (eds) *Europa*. University of Arizona Press, Tucson, pp 485–505
- McPhate JB, Darling NT, Curtis TL, Paw UC, Vo C, Graves G, Siegmund OWH, Ertley C (2019) Life testing of conventional and atomic layer deposition functionalized microchannel plates. In: *Proc. SPIE* 11118, UV, X-ray, and gamma-ray space instrumentation for astronomy XXI, 111180P. <https://doi.org/10.1117/12.2529517>
- Meitzler R, Jun I, Blase R, et al (2023) Investigating Europa's radiation environment with the Europa Clipper radiation monitor. *Space Sci Rev* 219:61. <https://doi.org/10.1007/s11214-023-01003-8>
- Nerney EG, Bagenal F (2020) Combining UV spectra and physical chemistry to constrain the hot electron fraction in the Io plasma torus. *J Geophys Res Space Phys* 125(4):e2019JA027458
- Nerney EG, Bagenal F, Steffl AJ (2017) Io plasma torus ion composition: Voyager, Galileo, and Cassini. *J Geophys Res Space Phys* 122(1):727–744
- Nimmo F, Bills BG, Thomas PC (2011) Geophysical implications of the long-wavelength topography of the Saturnian satellites. *J Geophys Res* 116(11):1–12. <https://doi.org/10.1029/2011JE003835>
- Ojakangas GW, Stevenson DJ (1989) Polar wander of an ice shell on Europa. *Icarus* 81:242–270. [https://doi.org/10.1016/0019-1035\(89\)90053-5](https://doi.org/10.1016/0019-1035(89)90053-5)
- Paganini L, Villanueva GL, Roth L, Mandell AM, Hurford TA, Retherford KD, Mumma MJ (2020) A measurement of water vapour amid a largely quiescent environment on Europa. *Nat Astron* 4:266. <https://doi.org/10.1038/s41550-019-0933-6>
- Pappalardo RT, Buratti BJ, Korth H, et al (2024) Science overview of the Europa Clipper Mission. *Space Sci Rev* 220:40. <https://doi.org/10.1007/s11214-024-01070-5>
- Raut U, Karne PL, Retherford KD, Davis MW, Liu Y, Gladstone GR, Patrick EL, Greathouse TK, Hendrix AR, Mokashi P (2018b) Far-ultraviolet photometric response of Apollo soil 10084. *J Geophys Res, Planets* 123:5. <https://doi.org/10.1029/2018JE005567>
- Raut U, Karnes PL, Retherford KD, Davis MW, Gladstone GR, Greathouse TK, Walther B, Czajka E (2018a) Performance and design of MgF₂ + Au coatings on aluminum mirrors: enabling far-ultraviolet solar occultation measurements for Europa-UVS. In: *Proc. SPIE* 10699 space telescopes and instrumentation 2018: ultraviolet to gamma ray 106992Z. <https://doi.org/10.1117/12.2312928>
- Raut U, Teolis BD, Mamo BD, Tucke OJ, Becker TM, Molyneux PM, Retherford KD, Greathouse TK, Gladstone GR (2023) Radiation darkening of Europa's cryoplume fallouts. *LPI Contrib* 2806:2299
- Retherford KD, Gladstone GR, Persyn SC, Davis MW, Greathouse TK, Molyneux PM, et al (2025) The Ultraviolet Spectrograph on ESA's Jupiter Icy Moon Explorer Mission (JUICE-UVS). *Space Sci Rev* (in prep)
- Roberts JH, McKinnon WB, Elder CM, et al (2023) Exploring the interior of Europa with the Europa Clipper. *Space Sci Rev* 219(6):46. <https://doi.org/10.1007/s11214-023-00990-y>
- Roth L (2021) A stable H₂O atmosphere on Europa's trailing hemisphere from HST images. *Geophys Res Lett* 48:e2021GL094289. <https://doi.org/10.1029/2021GL094289>
- Roth L, Retherford KD, Sau J, Strobel DF, Feldman PD, McGrath MA, Nimmo F (2014b) Orbital apocenter is not a sufficient condition for HST/STIS detection of Europa's water vapor aurora. *Proc Natl Acad Sci* 111:E5123–E5132. <https://doi.org/10.1073/pnas.1416671111>
- Roth L, Saur J, Retherford KD, Strobel DF, Feldman PD, McGrath MA, Nimmo F (2014a) Transient water vapor at Europa's south pole. *Science* 343:171–174. <https://doi.org/10.1126/science.1247051>
- Roth L, Saur J, Retherford KD, Strobel DF, Feldman PD, McGrath MA, Spencer JR, Blöcker A, Ivchenko N (2016) Europa's far ultraviolet oxygen aurora from a comprehensive set of HST observations. *J Geophys Res Space Phys* 121:2143–2170. <https://doi.org/10.1002/2015JA022073>
- Roth L, Retherford K, Ivchenko N, Schlatter N, Strobel DF, Becker TM, Grava C (2017) Detection of a hydrogen corona in HST Ly α images of Europa in transit of Jupiter. *Astron J* 153:67. <https://doi.org/10.3847/1538-3881/153/2/67>
- Saur J, Strobel DF, Neubauer FM (1998) Interaction of the Jovian magnetosphere with Europa: constraints on the neutral atmosphere. *J Geophys Res* 103(E9):19,947–19,962
- Schilling N, Neubauer FM, Saur J (2007) Time-varying interaction of Europa with the Jovian magnetosphere: constraints on the conductivity of Europa's subsurface ocean. *Icarus* 192:41–55
- Siegmund OWH, McPhate JB, Curtis T, Darling N, Vallerga JV, Cremer T, Ertley C (2020) Development of UV imaging detectors with atomic layer deposited microchannel plates and cross strip readouts. In: *Proc SPIE* 11454 X-ray, optical, and infrared detectors for astronomy IX 114541H. <https://doi.org/10.1117/12.2561753>

- Slater DC, Stern SA, Booker T, Scherrer J, A'Hearn MF, Bertaux JL, Feldman PD, Festou MC, Siegmund OHW (2001) Radiometric and calibration performance results for the Rosetta UV imaging spectrometer ALICE. In: Proc SPIE 4498, UV/EUV and Visible Space Instrumentation for Astronomy and Solar Physics, pp 239–247. <https://doi.org/10.1117/12.450059>
- Slater DC, Davis MW, Olkin CB, Scherrer J, Stern SA (2005) Radiometric performance of the New Horizons' ALICE UV imaging spectrograph. In: Proc. SPIE 5906, Astrobiology and Planetary Missions 590619. <https://doi.org/10.1117/12.613127>
- Smith HT, Mitchell DG, Johnson RE, Mauk BH, Smith JE (2019) Europa neutral torus confirmation and characterization based on observations and modeling. *Astrophys J* 871:69. <https://doi.org/10.3847/1538-4357/aaed38>
- Smith HT, Koga R, Tsuchiya F, Dols VJ (2022) Insight into Io enabled by characterization of its neutral oxygen torus. *J Geophys Res Space Phys* 127:e2022JA030581. <https://doi.org/10.1029/2022JA030581>
- Sparks WB, Hand KP, McGrath MA, Bergeron E, Cracraft M, Deustua SE (2016) Probing for evidence of plumes on Europa with HST/STIS. *Astrophys J* 829:121. <https://doi.org/10.3847/0004-637X/829/2/121>
- Sparks WB, Schmidt BE, McGrath MA, Hand KP, Spencer JR, Cracraft M, Deustua SE (2017) Active cryovolcanism on Europa? *Astrophys J* 839:L18. <https://doi.org/10.3847/2041-8213/aa67f8>
- Steffl AJ, Bagenal F, Stewart AI (2004) Cassini UVIS observations of the Io plasma torus. II. Radial variations. *Icarus* 172:91–103
- Stern SA, Slater DC, Gibson W, Scherrer J, A'Hearn M, Bertaux J-L, Feldman PD, Festou MC (1998) ALICE: an ultraviolet imaging spectrometer for the Rosetta orbiter. *Adv Space Res* 21:1517–1525. <https://doi.org/10.1007/s11214-008-9407-3>
- Stern SA, Scherrer J, Slater DC, et al (2005) ALICE: the ultraviolet imaging spectrograph aboard the New Horizons Pluto mission spacecraft. *Proc SPIE* 5906:358–367
- Stern SA, Slater DC, Scherrer JR, Stone JM, Dirks GJ, Versteeg MH, Davis MW, Gladstone GR, Parker J, Young LA, Siegmund OHW (2008) Alice, the ultraviolet imaging spectrograph aboard the New Horizons Pluto-Kuiper Belt mission. *Space Sci Rev* 140:155–187. <https://doi.org/10.1007/s11214-008-9407-3>
- Szalay JR, Smith HT, Zirnstein EJ, McComas DJ, Begley LJ, Bagenal F, et al (2022) Water-group pickup ions from Europa-genic neutrals orbiting Jupiter. *Geophys Res Lett* 49:e2022GL098111. <https://doi.org/10.1029/2022GL098111>
- Teolis BD, Wyrick DY, Bouquet A, Magee BA, Waite JH (2017) Plume and surface feature structure and compositional effects on Europa's global exosphere: preliminary Europa mission predictions. *Icarus* 284:18. <https://doi.org/10.1016/j.icarus.2016.10.027>
- Tosi F, et al (2024) Characterization of the surfaces and near-surface atmospheres of Ganymede, Europa and Callisto by JUICE. *Space Sci Rev* 220:59. <https://doi.org/10.1007/s11214-024-01089-8>
- Trumbo S, Brown ME (2023) The distribution of CO₂ on Europa indicates an internal source of carbon. *Science* 381:1308–1311. <https://doi.org/10.1126/science.adg4155>
- Turtle EP, McEwen AS, Patterson GW et al (2024) The Europa Imaging System (EIS) investigation. *Space Sci Rev* 220. <https://doi.org/10.1007/s11214-024-01115-9>
- Van Hoolst TG, Tobie G, Vallat C, Altobelli N, Bruzzone L, Cao H, Iess L, Kimura J, Khurana K, Dirx D, Genova A, Hussmann H, Lucchetti A, Mitri G, Moore W, Saur J, Stark A, Vorburger A, Wieczorek M, Aboudan A, Bergman J, Bovolo F, Breuer D, Cappuccio P, Carrer L, Cecconi B, Choblet G, De Marchi F, Fayolle M, Fienga A, Futaana Y, Hauber E, Kofman W KA, Lainey V, Molyneux P, Mousis O, Plaut J, Puccio W, Retherford K, Roth L, Seignovert B, Steinbrügge G, Thakur S, Tortora P, Tosi F, Zannoni M, Barabash S, Dougherty M, Gladstone R, Gurvits LI, Hartogh P, Palumbo P, Poulet F, Wahlund J-F, Grasset O, Witasse O (2024) Geophysical characterization of the interiors of Ganymede, Callisto and Europa by ESA's Jupiter ICy moons Explorer. *Space Sci Rev* 220:54. <https://doi.org/10.1007/s11214-024-01085-y>
- Vance SD, Craft KL, Shock E, et al (2023) Investigating Europa's habitability with the Europa Clipper. *Space Sci Rev* 219:81. <https://doi.org/10.1007/s11214-023-01025-2>
- Velez MA, Retherford KD, Hue V, Kammer JA, Becker TM, Gladstone GR, Davis MW, Greathouse TK, Molyneux PM, Brooks SM, Raut U, Versteeg MH (2024) Catalog of Ultraviolet Bright Stars (CUBS): Strategies for UV Occultation Measurements, Planetary Illumination Modeling, and Sky Map Analyses Using Hybrid IUE–Kurucz Spectra. *Planet Sci J* 5:93. <https://doi.org/10.3847/PSJ/ad0e70>
- Villanueva GL, Hammel HB, Milam SN, Faggi S, Kofman V, et al (2023) Endogenous CO₂ ice mixture on the surface of Europa and no detection of plume activity. *Science* 381:1305–1308. <https://doi.org/10.1126/science.adg4270>
- Waite JH Jr, et al (2006) Cassini ion and Neutral Mass Spectrometer: Enceladus plume composition and structure. *Science* 311(5766):1419–1422. <https://doi.org/10.1126/science.1121290>
- Waite JH, et al (2017) Cassini finds molecular hydrogen in the Enceladus plume: evidence for hydrothermal processes. *Science* 356(6334):155–159. <https://doi.org/10.1126/science.aai8703>

- Waite JH, Burch JL, Brockwell TG, et al (2024) MASPEX-Europa: the Europa Clipper neutral gas mass spectrometer investigation. *Space Sci Rev* 220:30. <https://doi.org/10.1007/s11214-024-01061-6>
- Westlake JH, McNutt RL, Grey M, et al (2023) The Plasma Instrument for Magnetic Sounding (PIMS) on the Europa Clipper spacecraft. *Space Sci Rev* 219:62. <https://doi.org/10.1007/s11214-023-01002-9>
- Windt DL (1998) IMD—software for modeling the optical properties of multilayer films. *Comput Phys* 12:360–370. <https://doi.org/10.1063/1.168689>
- Witasse O, the JUICE Teams (2020) JUICE (Jupiter Icy Moon Explorer): a European mission to explore the emergence of habitable worlds around gas giants. In: *Europlanet Science Congress 2020*, online, 21 September–9 Oct 2020, EPSC2020-76. <https://doi.org/10.5194/epsc2020-76>

Publisher's Note Springer Nature remains neutral with regard to jurisdictional claims in published maps and institutional affiliations.

Authors and Affiliations

K.D. Retherford^{1,2}  · T.M. Becker^{1,2} · G.R. Gladstone^{1,2} · T.K. Greathouse¹ · M.W. Davis¹ · M.A. Velez^{2,1} · M.A. Freeman¹ · S.M. Brooks³ · S. Ferrell¹ · R.S. Giles¹ · A.R. Hendrix⁴ · V. Hue⁵ · E. Johnson¹ · J.A. Kammer¹ · A.D. Marinan³ · B. D Mamo^{2,1} · M.A. McGrath⁶ · P.M. Molyneux¹ · E.G. Nerney⁷ · B. Perez¹ · K.B. Persson¹ · S. Pope¹ · U. Raut^{1,2} · R. Rickerson¹ · L. Roth⁸ · J. Saur⁹ · O.H. W Siegmund¹⁰ · J.R. Spencer¹¹ · A.J. Steffl¹¹ · S.A. Stern¹¹ · B.J. Trantham¹ · M.H. Versteeg¹ · J. Winkens⁹

✉ K.D. Retherford
kretherford@swri.edu

¹ Southwest Research Institute, San Antonio, TX, USA

² University of Texas at San Antonio, San Antonio, TX, USA

³ Jet Propulsion Laboratory, California Institute of Technology, Pasadena, CA, USA

⁴ Planetary Science Institute, Tucson, AZ, USA

⁵ Aix Marseille Université, CNRS, LAM (Laboratoire d'Astrophysique de Marseille), Marseille, France

⁶ SETI Institute, Mountain View, CA, USA

⁷ LASP, University of Colorado at Boulder, Boulder, CO, USA

⁸ KTH Royal Institute of Technology, Stockholm, Sweden

⁹ Universität zu Köln, Cologne, Germany

¹⁰ Sensor Sciences LLC, Pleasant Hill, CA, USA

¹¹ Southwest Research Institute, Boulder, CO, USA